Available online at www.sciencedirect.com
SCIENCE DIRECT®
Precambrian Research 122 (2003) 111–140
Precambrian Research
www.elsevier.com/locate/precamres

Neoproterozoic tectonic evolution of the northwestern Yangtze craton, South China: implications for amalgamation and break-up of the Rodinia Supercontinent

Wenli Ling [a,b,*], Shan Gao [c,b], Benren Zhang [b], Huimin Li [d], Ying Liu [a], Jianping Cheng [b]

[a] *Guangzhou Institute of Geochemistry, Chinese Academy of Sciences, Guangzhou 510640, PR China*
[b] *Faculty of Earth Sciences, China University of Geosciences, Wuhan 430074, PR China*
[c] *Key Laboratory of Continental Dynamics, Department of Geology, Northwest University, Xi'an 710069, PR China*
[d] *Tianjin Institute of Geology and Mineral Resources, Tianjin 300170, PR China*

Abstract

Three suites of Neoproterozoic igneous rocks (the Xixiang arc volcanic rocks, the Tiechuanshan bimodal basalt–rhyolite succession and the Wangjiangshan Gabbro) along the northwestern margin of the Yangtze craton in the Hannan area have been investigated. Single-grain zircon U–Pb TIMS dating of dacite and rhyolite indicates that the lower and upper units of the Xixiang Group erupted at 950 ± 4 and 895 ± 3 Ma, respectively, whereas the Tiechuanshan Formation was extruded at 817 ± 5 Ma. A set of radiometric constraints suggest that the Wangjiangshan Gabbro was formed at ca. 820 Ma.

The lower Xixiang unit is dominated by high-Mg andesite and low-Ti tholeiite. These rocks are characterized by high Mg numbers (69–73), Cr (209–621 ppm) and Ni (98–171 ppm), low TiO_2 (0.47–0.69 wt.%), depletion in LREE (La_N/Yb_N = 0.4–1.1) and variable negative anomalies of high strength field elements HFSE (Th, Nb, Ta Zr, Hf, P, and Ti). Together with high positive ε_{Nd} (950 Ma) values (+6.0 to +8.8), these features show an affinity of boninitic associations, which are usually found in fore-arc settings. The upper Xixiang unit ranges in lithology from basalt through andesite to dacite–rhyolite with ascending order. The rocks are characterized by enrichment in LREE (La_N/Yb_N = 1.70–7.75) and large ion lithophile elements and having pronounced negative Nb, Ta, Ti and Eu anomalies. Their ε_{Nd} (897 Ma) values range from +2.0 to +6.8. These features characterize modern arc volcanic suites. Rhyolite from the top of the Xixiang Group has a back-arc affinity as indicated by their high Na_2O and K_2O contents and LILE/HFSE ratio.

The Tiechuanshan Formation consists of bimodal basalt and rhyolite–dacite with a silica gap between 49.8 and 66.3 wt.%. The basalt shows variable negative Nb and Ta anomalies, and can be divided into tholeiitic and alkaline members with ε_{Nd} (817 Ma) being +4.6 to +5.3 and +0.2 to +3.8, respectively. The tholeiites exhibit primitive mantle-normalized incompatible elemental patterns resembling that of E-MORB along with high Cr (190–291 ppm), Ni (65–93 ppm) and Mg numbers (69–54). The alkaline basalts, on the other hand, display oceanic island basalt (OIB)-like incompatible elemental distributions characterized by enrichment in LILE and TiO_2 (2.59–1.91 wt.%) together with lower Mg numbers (46–17). The Tiechuanshan rhyolites and dacites are characterized by remarkable negative Eu (Eu/Eu^* = 0.37–0.73), Nb, Ta and Ti anomalies, high La_N/Yb_N (10.9–16.7), negative ε_{Nd} (t) values (−2.5 to −4.9) and high initial $^{87}Sr/^{86}Sr$ (t) ratios (0.7054–0.7106). These characteristics indicate significant contributions of crustal components. The Tiechuanshan assemblage is similar to volcanic rocks developed in continental rifts and continental flood basalt (CFB) provinces, which are considered to be plume-related.

* Corresponding author. Tel.: +86-27-87481664.
E-mail address: wlling@cug.edu.cn (W. Ling).

0301-9268/02/$ – see front matter
doi:10.1016/S0301-9268(02)00222-X

The Wangjiangshan Gabbro is tholeiitic in composition and has low Rb, U, Th, Nb, Ta, Zr and Hf concentrations along with positive ε_{Nd} (820 Ma), which implies derivation from a previously depleted mantle source. The less fractionated samples show high MgO (9.34–8.96 wt.%), Cr (368–312 ppm) and Ni (201–185 ppm) and positive ε_{Nd} (t) values (+5.5 to +3.8). They suggest high degree partial melting of the source mantle under a relatively high geotherm compared to the coeval southeastern Australian Gairdner Dyke.

The ca. 80 Ma age difference, contrasting rock associations and distinct geochemical and isotopic compositions of felsic rocks between the upper Xixiang Group and the Tiechuanshan Formation, suggest their diverse tectonic settings of formation. It is thus inferred that the lower and upper units of the Xixiang Group were formed in fore-arc and back-arc settings, respectively, whereas the Tiechuanshan volcanic suite and the Wangjiangshan Gabbro were developed in a plume-related intra-continental rift setting. Therefore, the Xixiang and Tiechuanshan volcanic suites and the Wangjiangshan Gabbro reflect a tectonic evolution from arc to intra-continental rift in the Neoproterozoic along the northwestern margin of the Yangtze craton. The transition occurred at ca. 820 Ma. The Tiechuanshan mafic rocks are geochronologically and geochemically indistinguishable from the Gairdner Dyke and its volcanic equivalents from southeastern Australia. Coeval mafic-ultramafic and granitic plutons in southern South China have also been documented, and are interpreted to be plume-related as well. Accordingly, the Neoproterozoic tectonic evolution in the Hannan area and elsewhere in South China supports a Rodinia Supercontinent reconstruction model, in which an ascending superplume centered beneath South China at ~820 Ma triggered the rifting and break-up of the Rodinia Supercontinent, separating South China from southeastern Australia.

Keywords: Neoproterozoic; Continental arc; Intra-continental rifting; Tectonic evolution; Yangtze craton; Rodinia

1. Introduction

There has been increasing evidence for a late Mesoproterozoic Supercontinent, Rodinia, which is suggested to have assembled through Grenvillian (1.3–1.0 Ga) orogeny and broken up during the Neoproterozoic (Dalziel, 1991; Hoffman, 1991; Moores, 1991). Although Grenvillian subduction-related and Neoproterozoic (ca. 0.82–0.75 Ga) rift-related rock sequences have been identified on individual continents (e.g. Zhao et al., 1994; Li et al., 1995, 1999; Wingate et al., 1998; Li, 1999; Frimmel et al., 2001; Keppie et al., 2001; Rickers et al., 2001), models for the Rodinia reconstruction both on assembling configuration and break-up tectonic regime are still controversial. As the SWEAT (Southwest US–East Antarctic connection; Moores, 1991) configuration is difficult to reconcile different ages of the proposed mafic dykes for a coeval plume genesis in western North America and southeastern Australia (ca. 780 Ma versus 827 ± 6 Ma; Wingate et al., 1998), alternative models have been proposed. Li et al. (1995) and Li et al. (1996) presented an assembling scenario, in which the South China block was located between the Australia–East Antarctica and Laurentia. They further argued that the impingement of a plume-head, which centered beneath South China block, resulted in the rifting and break-up of Rodinia onset ~820 Ma (Li et al., 1999). It has long been recognized that the early Neoproterozoic (1000–750 Ma) is a period of extensive tectonic and magmatic activities and is referred to as the Jinningian Movement by Chinese geologists (Chen et al., 1991 and references therein). This is highlighted by recent studies of the Rodinia Supercontinent. It is considered that the Neoproterozoic tectonic history of South China might provide vital constraints on the reconstruction of Rodinia (Li et al., 1999).

The South China block and the North China craton are two major tectonic units in eastern China. They were finally coalesced with the formation of the Qinling-Dabie-Sulu ultrahigh pressure metamorphic belt in Triassic (Fig. 1; inset a). South China consists of the Yangtze craton in the northwest and the Cathaysia block in the southeast. They amalgamated along a Meso- to Neoproterozoic collision belt (Chen et al., 1991; Li and McCulloch, 1996). Geochronological and geochemical studies indicate that considerable part of the Yangtze basement was formed around 1000–800 Ma (Li, 1999 and references therein). For example, a Nd isotopic investigation of the Yangtze Neoproterozoic sedimentary rocks shows that there is a dramatic decrease in depleted mantle Nd model ages (T_{DM}) from 1.8 to 1.3 Ga in stratigraphic sections of

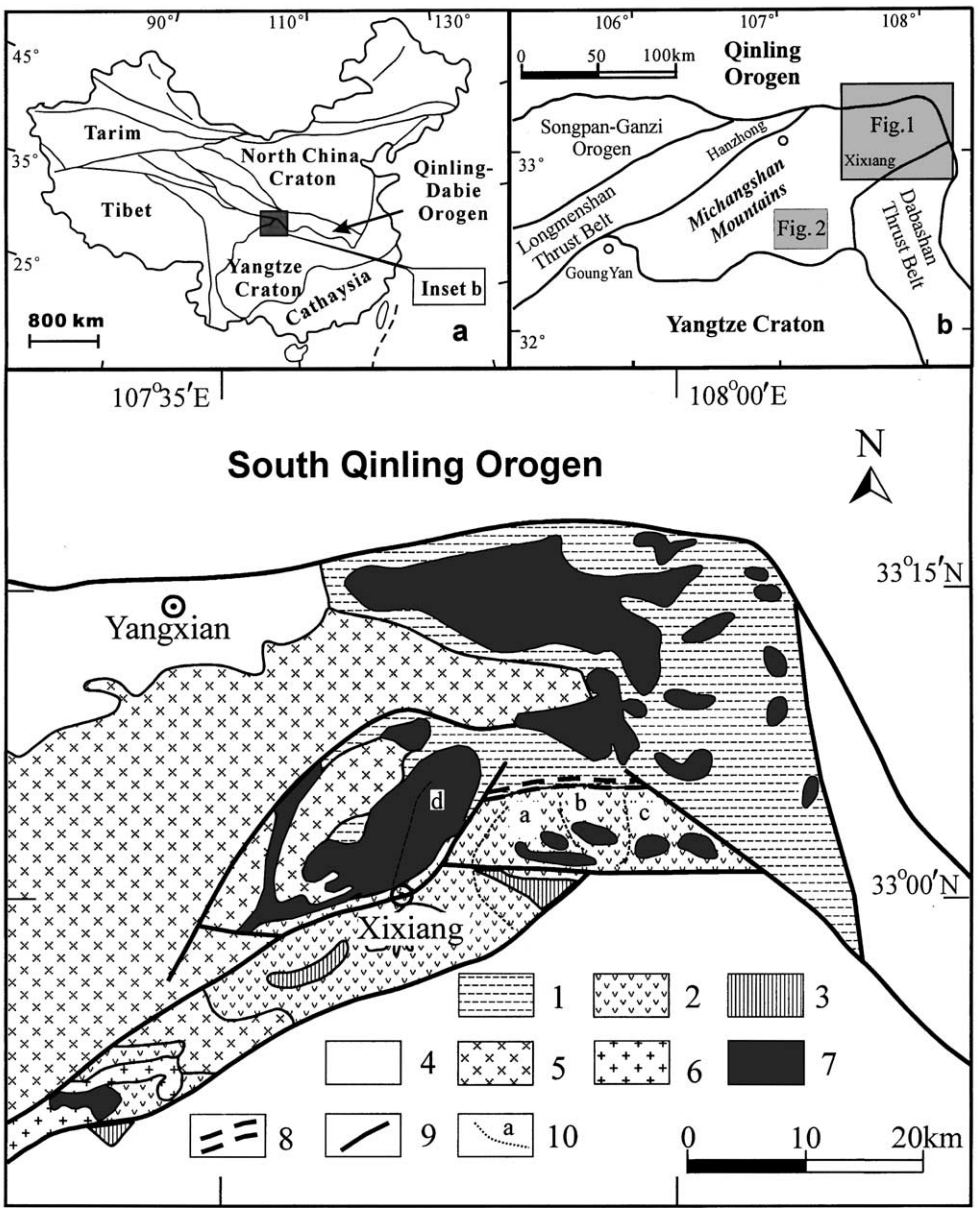

Fig. 1. Simplified geological map of the Xixiang region, northeastern Micangshan Mountains. Insets show tectonic location of the study area (gray box) in China (a) and the northwestern Yangtze craton (b). (1) Huodiya Group; (2) Xixiang Group; (3) Sinian sedimentary rocks; (4) Phanerozoic sedimentary cover; (5) diorite; (6) granite; (7) Gabbro; (8) ductile shear belt; (9) fault; and (10) sampling profile.

900–770 Ma, indicating a significant incorporation of juvenile crustal component due to rapid crustal uplift and erosion (e.g. Li and McCulloch, 1996). This period is also highlighted by eclogites and their host gneisses from the Qinling-Dabie-Sulu ultrahigh pressure metamorphic belt, which are products of Triassic continental subduction of the Yangtze craton beneath the North China craton. The eclogites and gneisses frequently show zircon U–Pb upper intercept ages of 830–750 Ma, which are interpreted to represent the

ages of their protolith (e.g. Ames et al., 1996; Hacker et al., 1998; Xie et al., 2001). However, the Meso- to Neoproterozoic tectonic evolution of the Yangtze craton is not well constrained. This is due partly to lack of precise age data for associated magmatic rocks and partly to scarcity of magmatic suites from the same area, which record individual episodes of the Jinningian tectonic evolution.

Ophiolitic suites of ca. 1.0 Ga have been recognized along the southeastern margin of the Yangtze craton (Zhou et al., 1990; Chen et al., 1991; Li et al., 1994; Guan et al., 1996). Accordingly, a model from continental arc to continental collision between the Cathaysia block and Yangtze craton has been advocated to explain the Neoproterozoic integration of these two units (Chen et al., 1991; Li, 1997; Li et al., 1997). However, these ophiolites are fragmental and difficult to use for studies of possible tectonic evolution through time, which is important for reasonable tectonic reconstructions.

Mafic to ultramafic dykes with the age of 828 ± 7 Ma have been recently documented in the southern Yangtze craton (Li et al., 1999). Granites associated with the dykes were dated at 826 ± 10 and 819 ± 9 Ma (Li, 1999), for which a co-magmatic and plume-related genesis was proposed (Li et al., 1999). The Suxiong bimodal volcanic rocks (803 ± 12 Ma) along the western margin of the Yangtze carton have also been argued to be plume-related (Li et al., 2002). These authors inferred that both the Gairdner Dyke Swarm of southeastern Australia (Zhao et al., 1994; Wingate et al., 1998) and the above Yangtze igneous suites might have been generated resulting from the development of a starting mantle plume within a wide continental rift setting, although the Suxiong Formation is ca. 25 Ma younger than the Gairdner Dyke Swarm (827 ± 6 Ma, Wingate et al., 1998). These studies provide evidence for a configuration of the South China connection between eastern Australia–Antarctica and Laurentia (Li et al., 1995).

The Hannan area, the Hanzhong administrative region in southern Shanxi Province, is located at the northeastern Micangshan Mountains along the northwestern margin of the Yangtze craton (Fig. 1; inset b). Two facts highlight its tectonic significance in Neoproterozoic studies of the South China. On the one hand, volcanic and plutonic rocks, which were formed in different tectonic settings and span between ca. 1.0 and 0.8 Ga in age, are well preserved there. They show clear evolution in rock association from island arc to intra-continental rifting (Gao et al., 1990, 1996). On the other hand, the northwestern margin of the Yangtze craton is regarded as a link between southeastern Australia and South China in Rodinia (Li et al., 1999). Therefore, the Neoproterozoic rocks along the northwestern margin of the Yangtze craton are expected to have recorded accretion and break-up of the eastern China continents in relation to the Rodinia Supercontinent. The Hannan igneous suites have been studied by Gao et al. (1990) and Ling (1996), and a generalized Proterozoic tectonic evolution model for the Qinling orogenic belt and adjacent Yangtze and North China cratons was proposed (Gao et al., 1996). However, timing of individual tectonic stages in the area is not well constrained due to rare precise age data.

This paper presents new zircon U–Pb ages and Sr–Nd isotopic and geochemical data for the associated Neoproterozoic volcanic and plutonic rocks in the Hannan area. The data are used to reconstruct the Neoproterozoic tectonic evolution of the northwestern margin of the Yangtze craton and constrain the amalgamation and break-up of the Rodinia Supercontinent.

2. Geological setting

Major and trace elemental compositions of the Xixiang Group, the Tiechuanshan Formation and the Wangjiangshan Gabbro are listed in Tables 5, 6 and 7, respectively. The Hannan area is situated at the northeastern Micangshan Mountains of the Shanxi Province along the northwestern margin of the Yangtze craton (Fig. 1). Pre-Sinian (>750 Ma) rocks are exposed in an area of about 1200 km^2 (Zhang, 1991) and can be divided into three tectonostratigraphic units. They are the Archean-Paleoproterozoic Houhe complex in the south and southwest in the Beiba–Goungyan area, the Meso- to Neoproterozoic Huodiya Group in the southwest in the vicinity of Beiba and in the northern Xixiang area, and the Neoproterozoic Xixiang Group in the northeast (Fig. 1). They are unconformably overlain by Sinian (750–540 Ma) and Phanerozoic unmetamorphosed sedimentary rocks.

The Houhe complex underwent upper amphibolite facies metamorphism and consists of trondhjemitic gneisses, amphibolites and migmatites with minor

marbles. Zircons from the felsic gneiss and migmatite yielded single-grain evaporation Pb–Pb ages of 2100–2600 Ma, which are similar to the Nd model age (T_{DM} = 2.2–2.9 Ga) of the gneiss and migmatite (Ling, 1996; Ling et al., 1997; Liu et al., 1997).

The Houhe complex is unconformably overlain by the greenschist-facies Huodiya Group, which can be divided into three units. The lower Mawozi and the middle Shangliang Formations are sequences of metasedimentary rocks. The upper Tiechuanshan Formation, which unconformably overlies the former two units (showing a fault contact in the Beiba area) and underlies the Sinian sedimentary rocks, is a bimodal basalt–dacite/rhyolite sequence with tuff and breccia in the upper part. The Tiechuanshan Formation shows a lot of similarity in petrological association with those of the Suxiong alkaline basaltic–rhyolitic suite (Li et al., 2002), which is located in the Sichuan Province, the west margin of the Yangtze craton and is some 700 km southwest of the Hannan area.

The Xixiang Group is a metavolcano-sedimentary succession and can be divided into two units (Gao et al., 1990). The lower unit consists of submarine low-K tholeiite and basaltic andesite and interbedded metasedimentary rocks. The upper unit is dominated by subaerial calc-alkaline to alkaline basaltic andesite, dacite, rhyolite with minor alkali basalt, which is overlain by a molasse sequence (Fig. 1). Zhang et al. (1997) reported a single-grain zircon evaporation $^{207}Pb/^{206}Pb$ age of 896 ± 13 Ma for an upper Xixiang rhyolite.

Voluminous contemporaneous ultramafic to felsic plutons were emplaced into the Xixiang (Fig. 1) and Huodiya Groups (Fig. 2). In the Hannan area, the Hannan Intrusive Complex consists of pyroxenite, Gabbro and norite (Wangjiangshan and Bijigou Gabbros), tonalite, trondhjemite, granodiorite and granite (Gao et al., 1990). Biotite from the Wangjiangshan Gabbro was dated at 1121 Ma by the $^{39}Ar/^{40}Ar$ method (Xia et al., 1988), while the granitoids give an age range of 1100–750 Ma by various isotopic methods (Gao et al., 1990, 1996; Ling, 1996; Zhang et al., 2000).

3. Analytical methods

About 120 samples of volcanic and plutonic rocks were taken from type sections of the Xixiang Group (Profiles a, b and c; Fig. 1), the Wangjiangshan Gabbro (Profile d; Fig. 1) and the Tiechuanshan Formation (Fig. 2). Of them 70 samples were selected for isotopic and geochemical analysis according to the freshness indicated by microscope and major elemental analyses. Zircons were separated from the lower Xixiang dacite (BMX-Zir), the upper Xixiang rhyolite (SJH-02) and the Tiechuanshan rhyolite (XG-02) by gravitational and magnetic techniques followed by hand picking. Under the SEM examination, no inherited core was found in the zircons. U–Pb isotopic analysis was conducted at the Tianjin Institute of Geology and Mineral Resources. For each of the three samples, a set of four analyses were made. Each analysis includes one to five zircon grains based on their length to width ratio. The analytical procedure is similar to that of Krogh (1973) and described in details in H.-M. Li et al. (1995).

Major elements were analyzed at Northwest University in Xi'an by XRF using glass disks and by traditional wet chemistry at the Analytical Center of Hubei Bureau of Geology and Mineral Resources in Wuhan. Analysis of international rock standards (BCR-2, GSR-1 and GSR-3) indicates analytical precision and accuracy both better than 5%.

Trace elements were analyzed using a Perkin-Elmer Sciex ELAN 6000 ICP-MS at the Guangzhou Institute of Geochemistry, Chinese Academy of Sciences and a POEMS III ICP-MS at China University of Geosciences in Wuhan. About 50 mg of sample powders were dissolved using a HF + HNO_3 mixture in a screw-top Savillex® Teflon beaker at ~100 °C for 7 days or in a home-made Teflon bomb at ~190 °C for 48 h. Analysis of USGS rock standards BCR-1, BCR-2, BHVO-1, and G-2 indicates precision and accuracy better than 2 and 10%, respectively, for most of the trace elements except transition metals. Detailed procedures for trace element analysis were described by Li et al. (1997) and Hu et al. (2000).

Sm–Nd isotopic compositions were determined using the ID-TIMS method by a multi-collector Finnigan MAT-261 mass spectrometer operated in static multi-collector mode at the Isotope Laboratory of the China University of Geosciences. Two aliquots of sample powder (200 meshes), ~100 mg each, were weighted. A mixture solution of ^{149}Sm and ^{145}Nd isotope spikes was weighted and added to one of the aliquots. Samples were digested in a Teflon bomb with a mixture of 1.5, 1 ml and five drops of concentrated

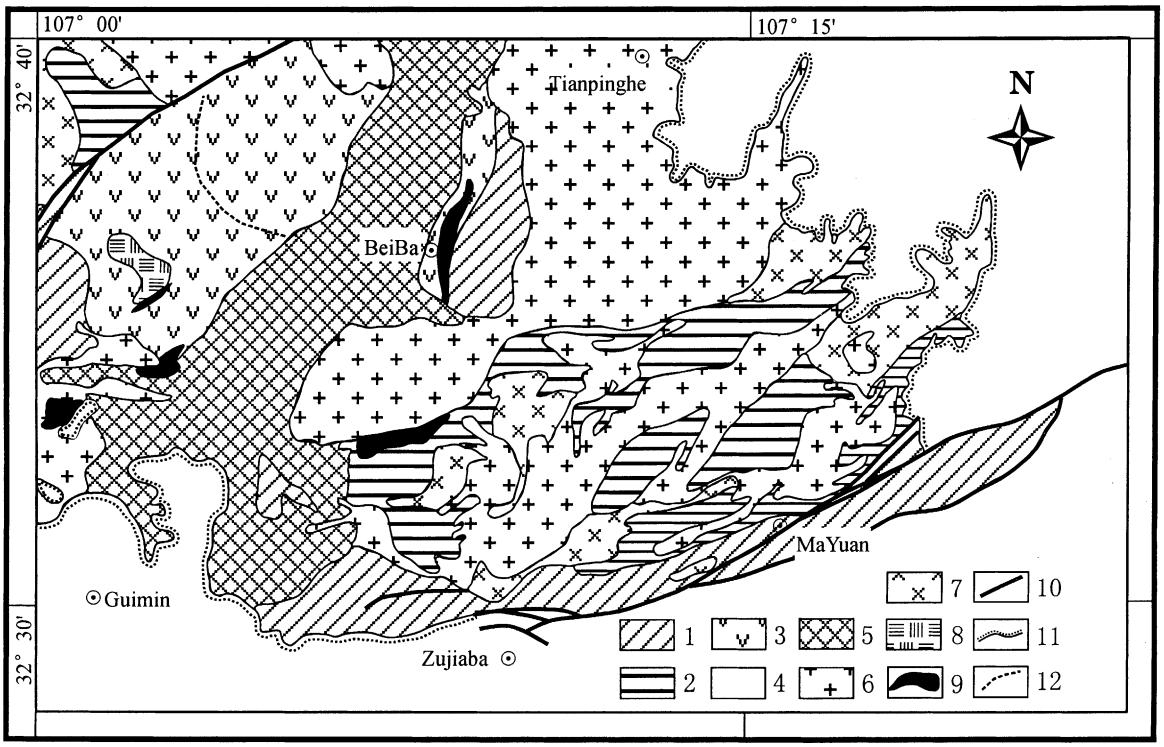

Fig. 2. Geological map of the Beiba area (modified after number 2 Team of the Geological Survey, Sichuan Bureau of Geology and Mineral Resources, 1970, unpublished). (1) Archean-Paleoproterozoic Houhe gneiss complex; (2) Meso-Neoproterozoic Mawozi and Shangliang Formations, lower and middle Huodiya Group; (3) Tiechuanshan volcanic-sedimentary succession, upper Huodiya Group; (4) Sinian and Phanerozoic sedimentary rocks; (5) Neoproterozoic Gabbro; (6) granite; (7) diorite; (8) alkaline granite; (9) mafic dike; (10) fault; (11) unconformity; and (12) sampling profile.

HF, HNO_3 and $HClO_4$, respectively. The sealed bombs were kept in an oven at 185 °C for 48 h. The decomposed samples were then dried on a hot plate, and converted into chlorides by adding concentrated $HClO_4$ and HCl in sequence. The re-dried salts of samples were dissolved again in 500 μl HCl and then loaded onto columns of AG50W-X8 and HDEHP resins sequentially for separation and purification of REE, and finally for separation of Nd and Sm by HCl eluant. The measured $^{143}Nd/^{144}Nd$ ratios were normalized to $^{146}Nd/^{144}Nd = 0.721900$. $^{143}Nd/^{144}Nd$ ratio of the La Jolla standard measured during the run has an average of 0.511862 ± 5 (2σ, $n = 15$). Analysis of BCR-2 gives $^{143}Nd/^{144}Nd = 0.512635 \pm 4$, $^{147}Sm/^{144}Nd = 0.1369$, Nd = 29.10 ppm, and Sm = 6.591 ppm, which agree well with recommended values for BCR-1 within analytical errors. Nd-Sr isotopic compositions of the Xixiang Group, the Tiechuanshan Formation and the Wangjiangshan Gabbro are listed in Tables 5, 6 and 7, respectively.

4. U–Pb and Sm–Nd ages

Zircons from the lower Xixiang dacite (BMX-Zir), the upper Xixiang rhyolite (SJH-02) and the Tiechuanshan rhyolite (XG-02) are generally homogeneous in color and morphology. They are light reddish, translucent, euhedral and elongated to short (length:width ratio is 2:5 for SJH-02 and XG-02 and 1:2 for BMX-Zir) with intact prisms and pyramids which are indicative of magmatic zircons (Fig. 3). Most of them range in size from 80 to 150 μm.

U–Pb isotopic compositions of the zircons are presented in Table 1 and plotted in the $^{207}Pb/^{235}U$ versus $^{206}Pb/^{238}U$ concordia diagrams in Fig. 4. As shown

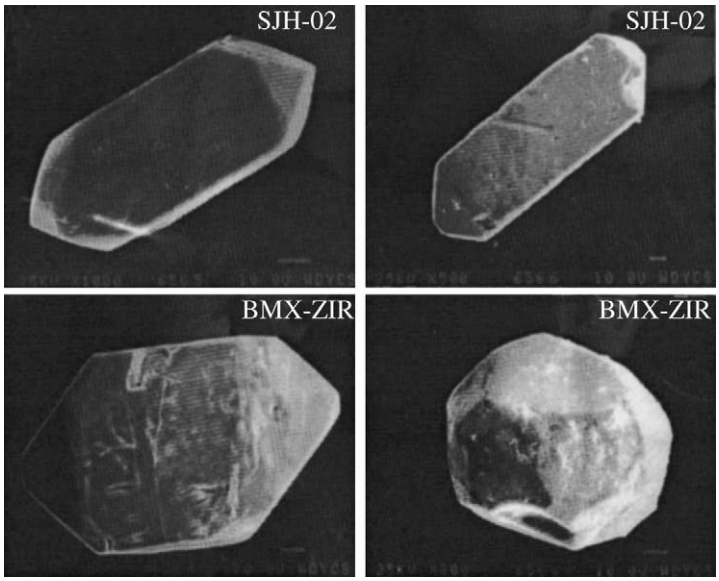

Fig. 3. SEM microphotograph of zircons.

in Fig. 4, zircons from the three samples are concordant or near-concordant. $^{206}Pb/^{238}U$, $^{207}Pb/^{235}U$ and $^{207}Pb/^{206}Pb$ ratios of BMX-Zir from the lower Xixiang Group have statistically indistinguishable weighted average ages of 946 ± 18, 949 ± 10 and 950 ± 12 Ma, respectively, yielding a concordant U–Pb age of 950 ± 4 Ma (2σ). Sample SJH-02 from the upper Xixiang Group gives weighted average $^{206}Pb/^{238}U$, $^{207}Pb/^{235}U$ and $^{207}Pb/^{206}Pb$ ages of 904 ± 18, 900 ± 12 and 895 ± 8 Ma, respectively, giving a concordant U–Pb age of 897 ± 3 Ma (2σ). Therefore, a ~53 Ma interval between the lower and upper units of the Xixiang Group is considered to reflect the approximate duration of the volcanism (Tables 2 and 3).

XG-02 from the Tiechuanshan Formation yields weighted average ages of 821 ± 7, 817 ± 6 and 806 ± 14 Ma, respectively, giving a concordant U–Pb age of 817 ± 5 Ma (2σ). This age is significantly younger than the ages of both BMX-Zir and SJH-02.

No zircon ages are available for the Wangjiangshan Gabbro. A linear trend of clinopyroxene + plagioclase + whole rock Sm–Nd isotopic composition, corresponding to an age of 785 ± 88 Ma (MSWD = 0.08) for sample WJS-1 was obtained by this study. However, this line seems to represent an errochron. The Wangjiangshan Gabbro is regarded as part of the Hannan Intrusive Complex consisting of pyroxenite, Gabbro (Wangjiangshan), norite, tonalite, trondhjemite, granodiorite and granite. Zhang et al. (2000) documented a Gabbro–tonalite–granite Sm–Nd isochron age of 837 ± 26 Ma for the Hannan Complex. Although within analytical errors this age is indistinguishable from the age of 785 ± 88 Ma by this study, the whole rock age is evidently more precise. Along with a consideration of the Tiechuanshan zircon U–Pb age, we suggest that the Wangjiangshan Gabbro is generated at or close to the timing of the Tiechuanshan Formation, i.e. ca. 820 Ma. This interpretation supports an Rb–Sr age of 825 ± 4 Ma for the Hannan granitoid batholith (Zhang et al., 2000).

5. Geochemistry

5.1. Xixiang volcanic rocks

Samples labeled with 55, 54 and BMX were collected from the lower Xixiang Group, while those with 52, 50 and SGH from the upper Xixiang Group. In SiO_2 versus $Na_2O + K_2O$ and Nb/Y versus Zr/TiO_2 classification diagrams for volcanic rocks (Fig. 5a and b; Winchester and Floyd, 1976; Middlemost, 1994), the Xixiang volcanic rocks range from basalt through

Table 1
U–Pb isotopic compositions of zircons from Xixiang Group and Tiechuanshan Formation

	Grain number	Weight (μg)	U (ppm)	Pb* (ppm)	Comm. Pb (ng)	$^{206}Pb/^{204}Pb$	$^{208}Pb/^{206}Pb$	Radiogenic ratios			Apparent age (Ma)[a]		
								$^{206}Pb/^{238}U$	$^{207}Pb/^{235}Th$	$^{207}Pb/^{206}Pb$	$^{206}Pb/^{238}U$	$^{207}Pb/^{235}Th$	$^{207}Pb/^{206}Pb$
BMX-Zir	1	~15	308	57	0.068	682	0.1602	0.1602 (16)	1.563 (21)	0.07073 (55)	958 (9)	955 (8)	950 (16)
	2	~15	156	29	0.037	629	0.1706	0.1590 (30)	1.552 (41)	0.07082 (118)	951 (17)	951 (16)	952 (34)
	3	~15	220	40	0.056	758	0.1590	0.1569 (23)	1.522 (37)	0.07035 (132)	940 (13)	939 (15)	939 (38)
	4	~15	141	24	0.009	2362	0.1645	0.1551 (34)	1.523 (47)	0.07120 (138)	930 (19)	940 (19)	963 (40)
											946 (18)[b]	949 (10)[b]	950 (12)[b]
SJH-02	1	~10	908	146	0.046	1836	0.1429	0.1493 (8)	1.420 (11)	0.06897 (32)	897 (5)	897 (5)	898 (10)
	2	~10	538	94	0.094	537	0.1581	0.1495 (13)	1.413 (19)	0.06857 (60)	898 (7)	894 (8)	886 (18)
	3	~10	267	44	0.009	2649	0.1686	0.1498 (27)	1.420 (33)	0.06876 (91)	900 (15)	898 (14)	891 (27)
	4	~10	237	40	0.020	1109	0.1574	0.1538 (21)	1.459 (28)	0.06880 (85)	922 (12)	913 (12)	893 (26)
											904 (18)[b]	900 (12)[b]	895 (8)[b]
XG-02	1	~10	263	44	0.057	407	0.1846	0.1367 (26)	1.241 (32)	0.06582 (100)	826 (15)	819 (14)	801 (32)
	2	~10	224	33	0.008	2456	0.1828	0.1350 (23)	1.232 (27)	0.06618 (81)	816 (13)	815 (12)	812 (26)
	3	~10	376	58	0.027	1186	0.1822	0.1360 (19)	1.237 (23)	0.06595 (71)	822 (11)	817 (10)	805 (22)
	4	~15	86	15	0.030	375	0.1812	0.1352 (54)	1.228 (65)	0.06590 (210)	817 (31)	814 (30)	803 (67)
											821 (7)[b]	817 (6)[b]	806 (14)[b]

$^{206}Pb/^{204}Pb$ ratios are corrected for whole procedure blanks (Pb = 0.050 ng; U = 0.002 ng) and spikes. Numbers in parentheses are errors reported as 2σ value to last digit(s).

[a] Weighted average at 95% confidence level.

[b] Weighted average of individual grains.

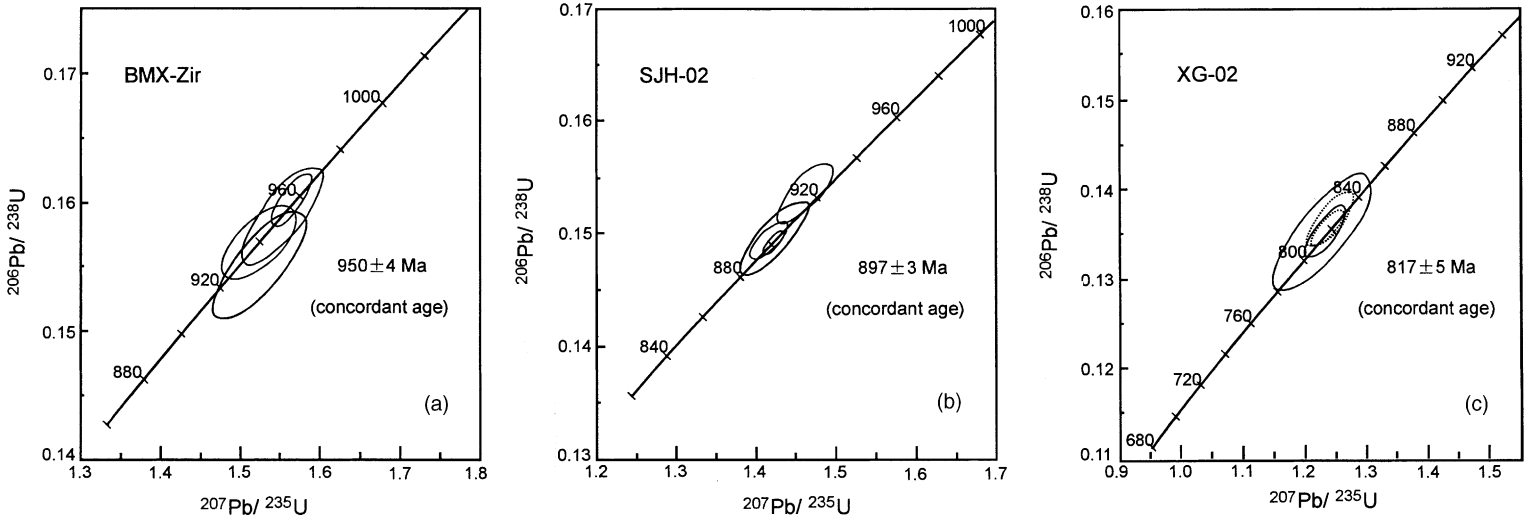

Fig. 4. U–Pb concordia diagrams for zircons of dacite BMX-Zir (a) and rhyolite SJH-02 (b) from the lower and upper units of the Xixiang Group and rhyolite TCS-02 (c) from the Tiechuanshan Formation. Because of the concordant nature of the data, the concordant ages calculated by $^{238}U/^{206}Pb$ and $^{207}Pb/^{206}Pb$ ratios using software ISOPLOT (Ludwig, 1998) are adopted to represent the ages of volcanic eruption.

Table 2
Chemical compositions of the Xixiang Group

Sample lithology	5002 RL	5006 RL	5008 BAD	5109 AD	5112 AD	SGH1 AD	SGH2 RL	5201 BT	5204 DC	5208 RL	5211 RL	5212 BAD	5215 TDC
In wt.%													
SiO_2	69.16	69.92	54.79	58.58	59.49	61.59	74.28	48.81	66.82	74.22	74.20	52.77	64.79
TiO_2	0.40	0.40	1.37	0.97	1.05	0.70	0.22	2.49	0.91	0.25	0.22	1.21	0.83
Al_2O_3	15.47	15.93	17.60	16.91	15.52	16.73	12.75	14.67	15.21	12.69	13.54	17.77	16.07
Fe_2O_3	2.67	2.26	7.99	6.09	4.24	2.37	1.10	8.19	1.37	3.05	1.60	3.95	1.27
FeO	0.25	0.13	0.91	1.18	2.53	3.33	1.38	5.50	2.86	0.34	0.18	4.36	2.86
MnO	0.04	0.03	0.15	0.12	0.14	0.11	0.04	0.23	0.12	0.13	0.03	0.16	0.11
MgO	0.30	0.43	3.13	4.24	5.60	2.01	0.21	4.65	1.25	0.10	0.10	3.41	1.28
CaO	0.25	0.43	5.39	1.84	1.35	3.51	0.47	7.77	1.84	0.24	0.24	7.22	2.33
Na_2O	3.60	4.84	3.29	3.04	4.16	5.66	4.20	2.50	5.76	3.73	4.06	4.53	4.84
K_2O	6.41	4.38	1.49	2.66	2.36	1.39	3.97	1.65	1.65	4.38	4.51	0.59	3.03
P_2O_5	0.09	0.08	0.26	0.20	0.23	0.17	0.02	0.22	0.28	0.02	0.01	0.43	0.28
CO_2	–	–	–	–	–	0.02	0.15	–	–	–	–	–	–
H_2O^+	1.04	0.86	3.29	3.86	3.33	2.20	0.96	2.95	1.59	0.92	0.75	3.27	1.60
Total	99.68	99.69	99.66	99.69	100.00	99.79	99.75	99.63	99.66	100.07	99.44	99.67	99.29
Mg numbers	20	31	46	59	66	45	16	45	40	7	12	49	42
In ppm													
Cr	2.71	0.79	113	102	83.6	27.0	4.44	131	7.23	2.02	2.31	64.5	4.34
Ni	–	–	56.7	47.8	37.5	15.4	–	19.2	0.94	–	–	26.9	–
Rb	170	131	31.3	105	52.1	36.6	104	69.8	73.5	106	152	27.1	84.9
Sr	201	175	361	158	148	373	105	384	414	48.7	40.3	751	461
Y	29.4	24.5	28.2	20.6	33.4	20.7	88.3	40.3	34.1	100	82.6	27.6	28.9
Zr	241	274	155	128	190	127	380	125	234	383	427	148	190
Nb	8.13	9.33	5.82	4.45	7.59	5.40	18.9	3.07	7.59	19.4	19.6	6.91	6.83
Cs	2.83	2.83	3.10	4.98	2.65	0.42	1.16	2.27	1.47	1.11	1.31	0.89	1.08
Ba	815	888	464	433	573	411	934	420	1300	763	751	497	1351
La	34.8	29.9	18.9	14.8	20.8	21.8	52.5	9.56	36.9	53.1	37.9	28.5	29.7
Ce	61.2	55.8	40.7	32.8	42.1	45.2	110	24.8	76.5	113	90.1	60.6	62.5
Pr	7.79	6.51	5.41	4.31	5.53	5.66	14.9	3.76	9.85	14.1	11.0	7.83	8.29
Nd	27.0	23.6	21.8	17.3	22.2	23.2	57.2	17.6	37.2	56.6	42.6	31.6	32.8
Sm	5.52	4.40	5.04	4.13	5.57	4.91	14.2	5.16	8.18	12.7	10.3	7.06	7.02
Eu	1.13	1.14	1.52	1.24	1.63	1.46	2.28	2.04	2.11	2.25	1.64	2.08	1.92
Gd	5.78	4.85	5.54	4.34	5.93	4.50	15.33	6.66	8.13	15.4	11.5	6.71	6.77
Tb	0.86	0.75	0.88	0.67	0.96	0.67	2.57	1.16	1.15	2.69	2.22	0.94	0.98
Dy	5.08	4.38	5.24	3.92	5.86	3.85	16.6	7.45	6.48	17.6	15.0	4.95	5.46
Ho	1.03	0.87	1.01	0.74	1.09	0.71	3.45	1.45	1.28	3.53	2.99	0.94	1.09
Er	3.09	2.56	2.91	2.22	3.22	2.10	10.34	4.16	3.77	10.6	9.41	2.71	3.08
Tm	0.47	0.41	0.43	0.31	0.49	0.32	1.53	0.59	0.56	1.60	1.52	0.38	0.46
Yb	3.34	2.78	2.82	2.05	3.15	2.00	10.38	3.79	3.74	10.2	10.3	2.49	3.06
Lu	0.50	0.44	0.42	0.33	0.46	0.31	1.59	0.58	0.56	1.53	1.63	0.40	0.49
Hf	6.91	7.56	4.24	3.42	4.91	3.48	12.5	3.62	6.61	11.8	13.8	3.51	5.72
Ta	0.78	0.84	0.42	0.34	0.53	0.34	1.39	0.25	0.49	1.34	1.46	0.40	0.43
Th	15.9	18.2	4.67	4.21	6.01	4.36	14.2	1.45	9.28	13.7	14.7	4.73	6.97
U	2.12	3.89	1.12	1.01	1.47	1.15	3.86	0.45	2.44	3.59	3.96	1.17	1.76

	5216 DC	5220 RL	5408 BT	5410 BAD	5413 AD	5414 BT	5415 DC	5503 BAD	5509 BAD	5516 BAD	5519 BT	5520 BAD	BMX1 BT	BMX2 BT
In wt.%														
SiO_2	68.46	74.82	50.35	56.37	57.65	48.93	64.24	53.54	56.65	52.12	49.00	53.07	48.54	50.94
TiO_2	0.78	0.21	0.65	0.47	1.07	1.41	0.69	1.70	1.67	1.37	0.64	0.58	0.69	0.56
Al_2O_3	15.74	13.05	14.78	12.82	13.67	16.53	16.76	13.24	13.63	16.69	12.67	13.08	17.36	15.59
Fe_2O_3	2.25	2.06	2.94	3.82	6.09	6.41	4.37	6.88	11.35	4.24	5.82	4.59	6.77	3.01
FeO	1.24	0.31	7.03	5.11	4.15	5.02	0.97	7.35	1.85	5.52	4.35	4.24	4.18	7.22
MnO	0.09	0.07	0.36	0.19	0.15	0.18	0.10	0.18	0.07	0.15	0.14	0.16	0.15	0.12
MgO	0.98	0.73	9.63	8.65	3.82	4.21	1.70	4.59	4.90	6.78	11.73	8.20	5.35	6.58
CaO	0.98	0.43	6.85	5.39	4.81	8.79	1.59	5.26	1.86	3.30	8.00	7.59	10.17	3.71
Na_2O	5.00	4.90	3.09	3.19	4.35	3.49	4.84	3.04	0.48	3.98	1.52	1.85	2.44	4.29
K_2O	2.46	1.90	0.10	0.20	0.26	0.14	1.74	0.39	3.35	0.60	0.45	2.75	0.04	0.86
P_2O_5	0.18	0.05	0.05	0.05	0.12	0.14	0.18	0.25	0.05	0.16	0.24	0.24	0.19	0.23
CO_2	–	–	–	–	1.09	1.16	–	–	0.04	0.04	0.04	–	0.04	2.12
H_2O^+	1.69	1.15	4.08	3.44	2.52	3.37	2.46	3.34	3.93	4.84	5.07	3.28	3.85	4.61
Total	99.85	99.68	99.91	99.70	99.75	99.78	99.64	99.76	99.83	99.79	99.67	99.63	99.77	99.84
Mg numbers	40	43	69	69	47	47	44	43	48	62	73	69	54	60
In ppm														
Cr	5.40	15.5	271	209	621	506	46.3	0.18	26.2	208	862	553	33.2	127
Ni	–	2.99	111	97.8	145	171	13.4	12.3	16.1	55.5	222	152	25.2	52.6
Rb	81.1	97.8	0.90	3.21	8.36	4.28	52.3	3.41	66.9	13.6	8.19	52.4	0.91	11.6
Sr	209	125	217	92.0	82.3	101	249	175	57.3	202	565	436	680	68.7
Y	35.3	64.7	16.7	15.6	32.9	30.3	22.0	47.9	28.5	31.0	13.3	12.7	13.31	13.0
Zr	270	160	17.5	13.4	47.0	67.9	111	151	123	126	39.6	42.2	41.0	39.9
Nb	8.44	16.4	1.15	0.63	2.77	3.62	6.79	13.4	6.13	4.18	2.61	2.49	2.54	2.00
Cs	2.04	2.36	0.10	0.11	0.52	0.19	2.12	0.12	2.15	0.58	0.19	0.71	0.03	0.36
Ba	999	440	45.4	48.1	76	35.2	599	91.9	178	112	173	1859	116	99.8
La	31.1	37.0	1.76	0.98	4.07	4.54	20.1	13.7	10.8	12.1	6.73	8.91	16.6	6.93
Ce	77.9	78.4	4.62	2.92	10.8	12.7	39.6	32.0	26.7	27.2	15.8	19.4	31.6	14.5
Pr	8.53	10.8	0.77	0.51	1.72	1.99	4.81	4.55	4.04	4.04	2.15	2.70	4.03	2.03
Nd	33.4	41.8	4.16	2.96	9.11	10.1	19.0	20.3	18.5	17.7	9.42	11.1	16.1	8.81
Sm	7.30	10.2	1.50	1.21	2.95	3.33	4.03	5.41	5.07	4.94	2.30	3.12	3.36	2.33
Eu	1.77	1.13	0.46	0.41	1.1	1.38	1.30	1.59	1.81	1.50	0.71	1.01	1.08	0.77
Gd	7.41	11.2	2.12	1.84	4.21	4.32	4.32	6.91	6.15	5.59	2.47	2.83	3.23	2.29
Tb	1.13	1.83	0.42	0.37	0.80	0.79	0.65	1.20	0.98	0.93	0.38	0.41	0.46	0.36
Dy	6.69	11.8	2.88	2.63	5.43	4.87	3.99	8.03	6.07	6.06	2.27	2.39	2.36	2.27
Ho	1.28	2.31	0.61	0.55	1.12	1.03	0.76	1.64	1.16	1.18	0.44	0.46	0.47	0.47
Er	4.02	7.15	1.81	1.66	3.11	2.97	2.34	5.10	3.30	3.34	1.30	1.37	1.39	1.37
Tm	0.59	1.12	0.28	0.24	0.49	0.45	0.37	0.76	0.48	0.51	0.20	0.21	0.20	0.21
Yb	3.89	7.35	1.82	1.66	2.99	2.88	2.47	5.23	3.06	3.34	1.31	1.38	1.29	1.44
Lu	0.62	1.07	0.28	0.26	0.46	0.43	0.40	0.78	0.45	0.49	0.21	0.21	0.20	0.22
Hf	7.79	6.23	0.68	0.56	1.34	2.07	3.48	4.06	3.41	3.63	1.19	1.28	1.11	1.00
Ta	0.55	1.30	0.08	0.05	0.18	0.24	0.44	0.94	0.37	0.31	0.15	0.15	0.13	0.11
Th	10.3	16.9	0.12	0.06	0.27	0.31	4.28	1.64	1.17	2.48	1.04	1.19	2.72	0.76
U	2.70	3.97	0.08	0.03	0.06	0.08	1.12	0.53	0.17	0.71	0.47	0.43	0.54	0.38

AD: andesite; BAD: basaltic andesite; BT: basalt; DC: dacite; RL: rhyolite; TDC: trachytic dacite. Mg number: $[Mg^{2+}/(Mg^{2+} + Fe^{2+})] \times 100$, assuming 80% of total Fe as Fe^{2+}. –below detection limits.

Table 3
Chemical compositions of the Tiechuanshan Formation

Sample lithology	4007 BT	4008 BT	4009 DC	4010 BT	4011 RL	4012 DC	4014 TDC	4015 RL	XG-01 RL	XG-02 RL	XG-03 TDC
In wt.%											
SiO_2	48.75	49.45	63.18	49.34	69.35	66.25	68.04	75.57	71.57	69.75	67.50
TiO_2	1.18	1.47	1.09	2.16	0.21	0.29	0.28	0.25	0.24	0.33	0.33
Al_2O_3	16.44	15.74	14.83	17.24	14.37	16.39	15.48	11.78	13.56	15.22	15.42
Fe_2O_{3t}	nd	nd	6.43	12.49	nd	2.65	nd	4.79	nd	nd	nd
Fe_2O_3	1.90	3.22	nd	nd	2.65	nd	3.67	nd	3.37	2.29	1.67
FeO	6.93	7.00	4.18	8.35	1.85	1.38	0.65	1.12	0.78	0.58	2.42
MnO	0.17	0.23	0.14	0.19	0.12	0.06	0.10	0.02	0.15	0.11	0.14
MgO	7.63	6.63	1.83	2.84	0.50	0.13	0.10	0.08	0.18	0.15	0.33
CaO	10.64	9.59	4.69	6.71	0.95	1.31	0.77	0.29	2.42	0.88	0.95
Na_2O	2.84	3.46	3.47	4.61	3.48	3.75	4.15	4.11	4.69	4.48	4.84
K_2O	0.75	1.00	2.10	1.36	5.15	6.13	5.46	2.96	1.72	5.24	4.84
P_2O_5	0.16	0.18	0.52	0.63	0.03	0.06	0.05	0.01	0.06	0.05	0.06
CO_2	–	–	nd	nd	–	nd	–	nd	0.43	0.02	0.30
H_2O^+	2.69	2.15	nd	nd	0.86	nd	0.54	nd	0.62	0.53	0.83
LOI	nd	nd	1.27	2.00	nd	1.00	nd	0.37	nd	nd	nd
Total	100.08	100.12	99.55	99.57	99.52	100.16	99.29	99.97	99.79	99.63	99.63
Mg numbers	66	60	41	36	21	11	5	4	10	11	16
In ppm											
Cr	291	270	26.7	46.1	1.68	1.56	4.26	5.08	6.86	8.27	7.51
Ni	88.3	79.9	25.4	34.0	0.86	1.64	0.94	2.41	1.44	1.37	1.23
Rb	32.1	35.8	35.3	25.0	150	102	170	54.5	73.0	162	149
Sr	235	270	246	144	142	37.4	88.8	12.5	108	112	97.2
Y	22.3	28.9	42.2	44.8	60.2	53.0	50.3	69.9	48.7	47.5	59.2
Zr	80.0	66.6	254	293	539	446	473	1466	382	468	482
Nb	2.86	4.55	18.7	16.8	32.9	30.3	33.3	45.6	33.0	31.6	34.7
Cs	1.26	0.62	0.75	0.67	0.82	0.92	2.54	0.25	1.33	2.43	1.08
Ba	130	359	738	813	833	1117	1559	62.0	758	2005	1642
La	6.87	8.49	39.0	40.9	109	135	140	62.0	94.2	130	155
Ce	15.6	20.6	78.9	84.9	196	266	242	129	173	231	284
Pr	2.29	2.91	10.1	10.9	21.4	28.1	26.4	15.1	19.1	24.5	29.5
Nd	10.3	12.9	42.7	45.1	74.0	93.6	87.8	55.2	60.8	81.0	95.8
Sm	2.98	3.73	9.01	9.13	13.2	13.9	13.4	10.2	11.1	13.0	15.7
Eu	1.21	1.33	2.16	2.45	1.58	1.95	2.14	0.33	1.72	2.26	2.61
Gd	3.45	4.43	8.91	9.26	12.3	11.3	13.1	10.0	10.7	12.5	15.1
Tb	0.63	0.80	1.39	1.48	1.82	1.81	1.75	1.90	1.55	1.66	2.02
Dy	3.98	5.00	7.91	8.74	10.5	10.4	9.59	12.4	8.57	8.88	10.8
Ho	0.84	1.04	1.62	1.77	2.14	2.07	1.94	2.67	1.77	1.73	2.2
Er	2.20	2.81	4.78	5.14	6.37	6.20	5.75	8.35	5.20	5.24	6.65

Tm	0.33	0.43	0.71	0.75	0.99	0.92	0.82	1.32	0.79	0.79	0.94
Yb	2.09	2.78	4.68	4.86	6.75	6.14	5.65	8.82	5.34	5.36	6.37
Lu	0.32	0.40	0.74	0.76	1.08	0.98	0.88	1.38	0.87	0.90	1.00
Hf	2.06	1.64	6.49	6.67	13.0	11.4	11.6	21.5	9.65	11.8	12.5
Ta	0.18	0.29	1.27	1.13	2.15	2.07	2.08	3.01	2.13	2.13	2.19
Th	0.91	0.83	5.84	5.26	18.4	20.7	19.7	28.5	16.4	19.1	19.3
U	0.26	0.21	1.91	1.52	4.14	3.51	2.89	3.49	3.28	3.49	4.28
	XG-04 BT	XG-05 BT	XG-06 BT	XG-7 BT	XG-8 BT	XG-9 BT	XG-10 BT	XG-11 BT	XG-12 BT	XG-13 BT	XG-14 TDC
In wt.%											
SiO_2	48.92	49.80	49.35	48.48	50.31	49.78	49.35	48.83	56.87	48.37	57.92
TiO_2	2.45	2.34	1.57	1.07	1.56	1.66	1.57	1.55	1.91	2.59	0.84
Al_2O_3	15.09	16.23	15.50	16.50	15.16	15.85	15.42	14.96	14.66	13.78	15.90
Fe_2O_{3t}	nd	nd	nd	9.01	11.77	12.14	11.58	11.70	10.62	15.55	12.93
Fe_2O_3	2.84	4.35	1.82	nd	nd	nd	nd	nd	nd	nd	nd
FeO	9.48	8.75	9.68	6.25	7.70	7.75	7.70	7.25	6.70	10.95	5.82
MnO	0.26	0.18	0.27	0.13	0.23	0.26	0.22	0.24	0.23	0.28	0.13
MgO	2.89	3.31	6.37	8.10	5.93	5.67	6.67	6.77	2.92	5.44	1.06
CaO	9.12	6.93	8.82	10.51	9.28	9.33	9.03	10.00	5.58	7.79	3.30
Na_2O	3.80	4.24	3.47	2.58	3.47	3.04	3.45	3.21	4.63	3.39	4.07
K_2O	1.92	1.58	0.72	0.76	0.48	0.87	0.78	0.74	0.87	1.19	2.60
P_2O_5	0.75	0.41	0.20	0.13	0.19	0.21	0.19	0.18	0.93	0.42	0.25
CO_2	0.35	0.02	0.02	nd	nd	nd	nd	nd	nd	nd	nd
H_2O^+	1.85	1.60	1.97	nd	nd	nd	nd	nd	nd	nd	nd
LOI	nd	nd	nd	2.30	1.23	1.38	1.27	1.36	1.44	1.17	1.23
Total	99.72	99.74	99.76	99.57	99.61	100.19	99.53	99.54	100.66	99.97	100.23
Mg numbers	35	37	56	69	56	54	59	59	41	46	17
In ppm											
Cr	8.44	5.03	219	271	229	190	222	234	6.04	44.4	5.18
Ni	13.5	6.69	77.2	92.7	85.2	65.3	87.2	89.2	4.52	32.6	5.87
Rb	65.3	50.0	23.6	31.0	15.2	31.2	26.1	23.7	23.9	35.3	36.2
Sr	344	365	334	222	318	399	273	312	247	267	251
Y	56.3	31.3	27.3	22.3	33.0	34.5	34.1	32.4	57.0	52.9	162
Zr	284	154	99.6	72.5	112	120	115	112	217	212	1036
Nb	22.6	14.5	4.97	2.68	5.01	5.50	4.93	4.79	11.3	13.3	72.5
Cs	0.55	1.96	0.48	1.38	0.34	0.38	0.45	0.43	0.39	0.44	0.51
Ba	1048	608	434	149	142	452	254	322	355	549	916
La	48.9	23.2	8.41	6.21	9.71	10.5	9.42	9.83	25.4	21.5	108
Ce	97.5	47.4	20.6	14.8	23.8	24.6	22.2	22.9	60.8	49.3	218
Pr	13.1	6.08	2.78	2.07	3.18	3.39	3.11	3.23	7.97	6.64	26.0
Nd	50.5	23.9	13.0	10.1	15.6	16.1	14.8	15.3	36.5	29.2	99.5
Sm	10.7	5.46	3.85	2.99	4.58	4.34	4.34	4.41	9.49	7.81	21.9

Table 3 (*Continued*)

Sample lithology	4007 BT	4008 BT	4009 DC	4010 BT	4011 RL	4012 DC	4014 TDC	4015 RL	XG-01 RL	XG-02 RL	XG-03 TDC
Eu	3.3	1.87	1.32	0.92	1.40	1.43	1.29	1.33	2.84	2.09	2.56
Gd	11.3	5.93	4.40	2.84	4.04	4.28	4.09	4.08	8.08	6.98	19.0
Tb	1.82	0.97	0.76	0.57	0.82	0.81	0.81	0.79	1.47	1.33	3.56
Dy	10.3	5.48	4.81	3.80	5.27	5.35	5.28	5.37	9.01	8.30	24.0
Ho	2.09	1.17	0.99	0.86	1.20	1.24	1.19	1.16	1.96	1.88	5.26
Er	5.78	3.35	2.75	2.20	3.28	3.40	3.33	3.30	5.33	5.14	15.2
Tm	0.88	0.49	0.40	0.34	0.48	0.47	0.49	0.47	0.71	0.74	2.33
Yb	5.51	3.20	2.51	2.24	3.08	3.24	3.31	3.19	5.03	4.99	17.4
Lu	0.84	0.49	0.4	0.33	0.49	0.52	0.49	0.47	0.74	0.77	2.66
Hf	6.21	3.49	2.45	2.18	3.00	3.29	2.90	3.10	5.58	5.65	25.5
Ta	1.39	0.96	0.32	0.18	0.28	0.32	0.29	0.29	0.81	0.88	4.45
Th	5.60	3.90	0.83	0.73	0.71	0.99	0.80	0.79	5.10	3.42	24.6
U	1.92	1.03	0.23	0.24	0.26	0.33	0.24	0.26	1.34	1.03	4.36

Fe_2O_{3t}: total iron as Fe_2O_3 determined by XRF; LOI: loss on ignition; nd: not determined.

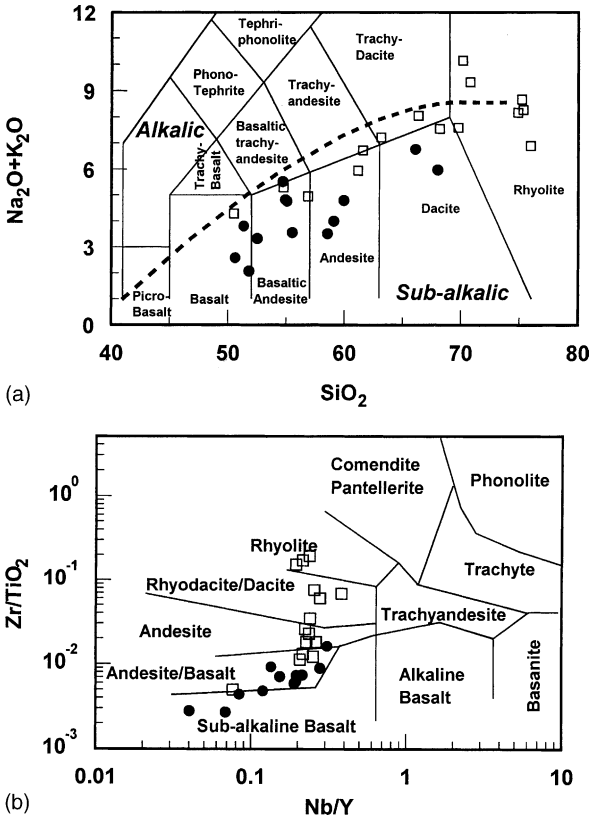

Fig. 5. $Na_2O + K_2O$ vs. SiO_2 (Middlemost, 1994) and Nb/Y vs. Zr/TiO_2 (Winchester and Floyd, 1976) diagrams for the Xixiang volcanic rocks. Filled circles and open squares denote the lower and upper Xixiang units, respectively.

andesite to rhyolite without a significant gap in SiO_2. The samples are subalkalic except two rhyolite samples 5002 and 5006 with the highest $Na_2O + K_2O$ (9.3–10.2 wt.%). The Xixiang Group also shows a clear lithological evolution from basalt and andesite in the lower unit to dacite and rhyolite in the upper unit (Fig. 5).

At given SiO_2 content, mafic rocks from the lower and upper units can be distinguished from each other in terms of trace element composition, MgO and TiO_2. Basalts (5408 and 5519) and andesites (5410 and 5520) from the lower unit are characterized by low concentrations for nearly all incompatible elements and variable magnitudes of negative anomalies in HFSE (Th, Nb, Ta, Zr, Hf, P and Ti) relative to neighboring REE (Fig. 6c and d). These characteristics are typical of boninite and associated low-Ti basalt found in subduction- or fore-arc-related settings of Phanerozoic Koh Massif (Cameron, 1989), Izu-Bonin (Arculus et al., 1992; Pearce et al., 1992), Mariana (Hickey-Vargas, 1989), Yukon-Tanana (Piercey et al., 2001) and Precambrian Abitibi, Canada (Kerrich et al., 1998). They are characterized by high Mg (MgO 8.20–11.73 wt.%; Mg numbers 69–73), Cr (209–862 ppm) and Ni (98–222 ppm) and low TiO_2 (0.47–0.65 wt.%) with a MORB-like REE pattern (La_N/Yb_N = 0.40–4.36). In a Mg number versus primitive mantle-normalized Nb/La ratio diagram (Sun and McDonough, 1989), the lower Xixiang rocks fall into the boninite and associated low-Ti tholeiite fields (Fig. 7; Kerrich et al., 1998).

In contrast, basalts and andesites from the upper Xixiang Group display remarkably higher LILE concentrations and higher LILE/HFSE and LILE/HREE ratios compared to the lower Xixiang rocks. Negative Nb, Ta, P and Ti anomalies are even more pronounced (Fig. 6a and b). They are also coupled by LREE enrichment (La_N/Yb_N = 1.70–7.75) and small negative Eu anomaly (Eu/Eu^* = 0.86–0.91). These mafic rocks show trace element signatures, which are similar to their intercalated felsic volcanic rocks with enrichment in LILE and LREE and depletion in Nb, Ta, P, Ti and Eu. These features are typical of island arc volcanic rocks as shown in Fig. 6a and b comparable with Japan Quaternary mafic and felsic arc volcanic rocks (Togashi et al., 2000).

Positive ε_{Nd} (t) values (+2.0 to +8.8) characterize all of the Xixiang mafic and felsic rocks. It is important to note that ε_{Nd} (t) (+6.0 to +8.8) of the boninites and associated low-Ti basalts from the lower unit are comparable with the upper limit (+8.0) of the depleted mantle at 950 Ma (Goldstein et al., 1984) and are significantly higher than the values of the mafic (+2.0 to +6.8) and felsic (+2.3 to +5.7) rocks from the upper unit.

5.2. Tiechuanshan volcanic suite

Bimodal volcanic succession characterizes the Tiechuanshan Formation. As shown in Fig. 8, all Tiechuanshan samples but 4009, XG-12 and XG-14 fall into the two distinct fields of basalt and dacite–rhyolite with a large SiO_2 gap between 50 and 66 wt.%. Moreover half of the samples are alkaline. The basalts can be further divided into tholeiitic

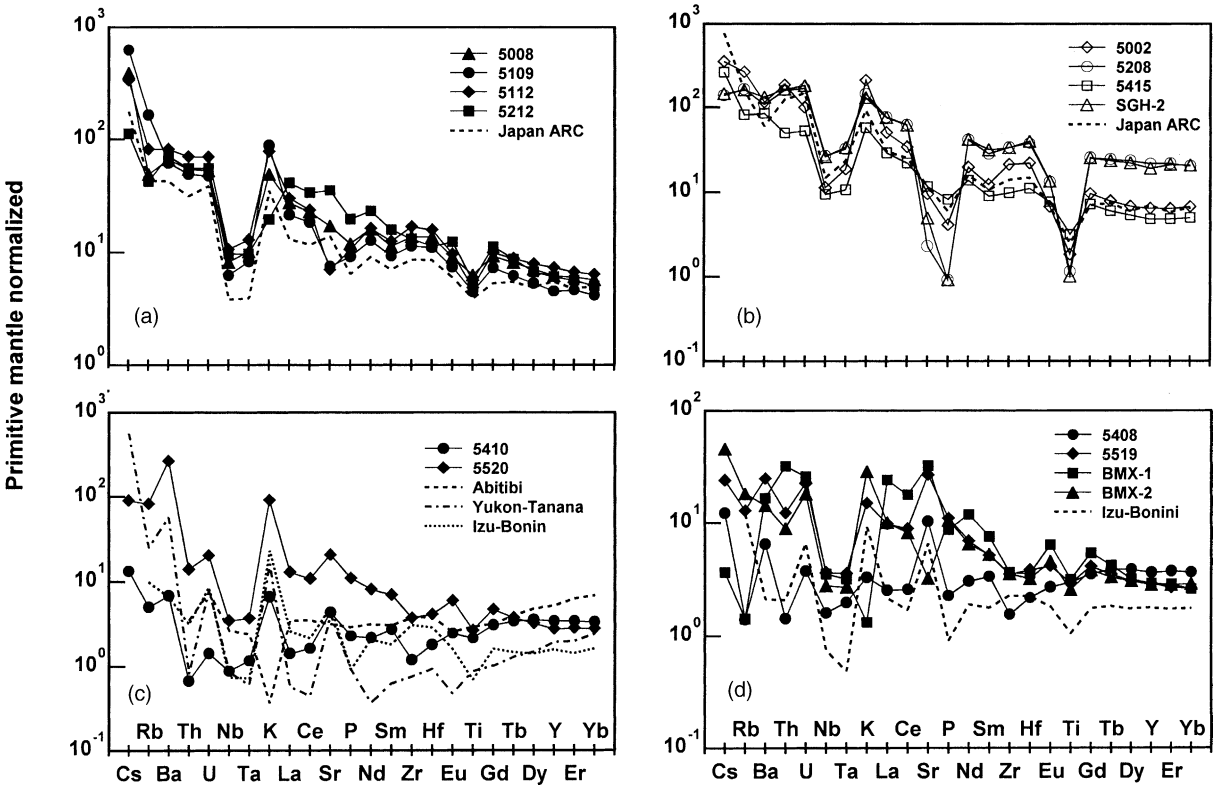

Fig. 6. Primitive mantle-normalized incompatible trace element distributions for the Xixiang Group of mafic (a) and felsic (b) volcanic rocks from the upper unit and boninitic (c) and low-Ti basaltic (d) rocks from the lower unit. Filled and open symbols denote basalt/andesite and rhyolite/dacite, respectively. The primitive mantle values are from Sun and McDonough (1989). Average compositions of Japan Quaternary mafic (a) and felsic (b) arc volcanic rocks are from Togashi et al. (2000), while those of boninites from Izu-Bonin, Yukon-Tanana and Abitibi (c) are from Arculus et al. (1992), Pearce et al. (1992), Piercey et al. (2001) and Kerrich et al. (1998), respectively. Low-Ti basalt data (d) are from Arculus et al. (1992) and Pearce et al. (1992).

and alkaline members based on $Na_2O + K_2O$ versus SiO_2 plot and the Zr/P_2O_5 versus TiO_2 discrimination diagram (Winchester and Floyd, 1976) (not shown). These two subtypes were collected from the lower and upper units of the Tiechuanshan Formation, respectively. The tholeiites (4007, 4008 and XG-6–11) show smooth chondrite-normalized REE patterns (Fig. 9a) with slight enrichment in LREE (La_N/Yb_N = 1.9–2.3) and insignificant to slightly positive Eu anomalies (Eu/Eu^* = 1.15–0.92). In contrast, the alkaline basalts (XG-4, -5, -12, -13, -14 and 4010) exhibit higher La_N/Yb_N (2.9–6.0, Fig. 9b) and negligible to prominent negative Eu anomalies (Eu/Eu^* = 1.0–0.38). Lower TiO_2 (1.07–1.66 wt.%), higher Mg numbers (54–69), Cr (190–291 ppm) and Ni (65–93 ppm) as well as higher ε_{Nd} (817 Ma) values (+4.6 to +5.3) of the tholeiites also distinguish them from the alkaline basalts, having Mg numbers 17–46, TiO_2 2.16–2.59 wt.%, Cr 5–43, Ni 5–33 ppm and ε_{Nd} (t) +0.20 to +3.8. These two types of basalts show incompatible element distributions similar to tholeiitic and alkaline basalts in continental rifts (Fig. 10). In Fig. 10a, the Tiechuanshan tholeiites show moderate enrichment in LILE and variable depletion in Nb, Ta and P, which resemble the Gairdner Dyke and its tholeiitic volcanic equivalents from southeastern Australia (Zhao et al., 1994) and tholeiites from the Siberian Traps (Hawkesworth et al., 1995). The tholeiitic rocks display E-MORB-like trace element distributions except for enrichment in LILE and depletion in Nb, Ta and P. The Tiechuanshan alkaline basalts (Fig. 10b), on the other hands, show patterns

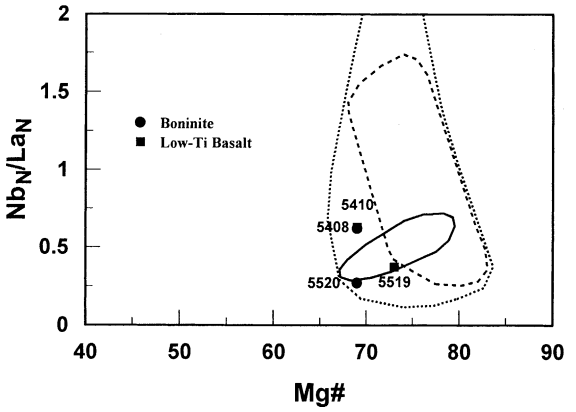

Fig. 7. Mg number vs. primitive mantle-normalized Nb/La ratio for the lower Xixiang mafic volcanic rocks (after Kerrich et al., 1998). Solid line and dashed line enclose fields of boninites defined by Hickey and Frey (1982) and Cameron (1989), respectively, and dotted line indicates Phanerozoic boninite and low-Ti basalt field (Kerrich et al., 1998). Primitive mantle values are from Sun and McDonough (1989).

analogous to high-Ti basalts and picrites from the Karoo (Gibson et al., 2000) and the Suxiong alkaline basalts (Li et al., 2002) with moderate depletion in Nb, Ta, Sr and Ti. The alkaline basalts are essentially similar to oceanic island basalt (OIB) in geochemical composition.

Negative Nb and Ta anomalies also typify the Tiechuanshan felsic rocks (Fig. 10c). Their Sr, Eu ($Eu/Eu^* = 0.37–0.73$), P and Ti are even more depleted than the continental crust (Rudnick and

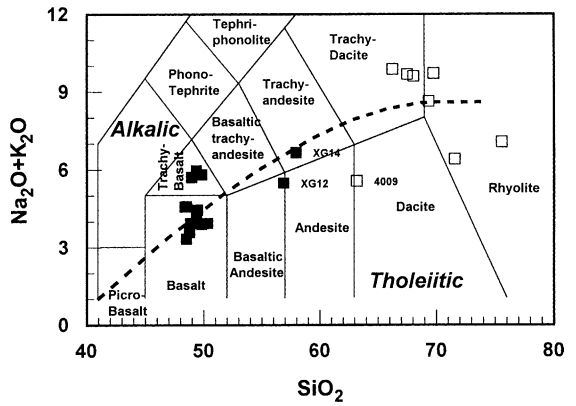

Fig. 8. $Na_2O + K_2O$ vs. SiO_2 plot (Middlemost, 1994) for the Tiechuanshan volcanic rocks. Filled and open symbols denote mafic and felsic rocks, respectively.

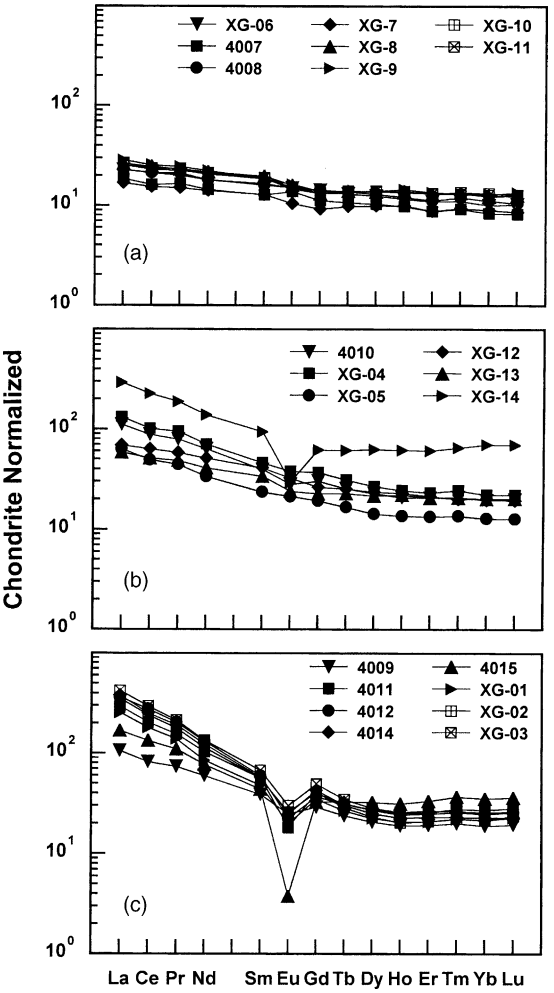

Fig. 9. Chondrite-normalized REE patterns for the Tiechuanshan tholeiites (a), alkaline basalts (b), and rhyolites (c). Chondrite values are from Sun and McDonough (1989).

Fountain, 1995). These features, along with high La_N/Yb_N (10.9–16.7, Fig. 9c) and LILE, indicate a highly evolved magma and are indistinguishable from those of Suxiong alkaline rhyolites (Li et al., 2002). It should be noted that the Tiechuanshan felsic rocks have negative ε_{Nd} (t) values (−2.5 to −4.9) and high initial $^{87}Sr/^{86}Sr$ (t) ratios (0.7054–0.7106). These are somewhat different from the Suxiong rhyolites, whose Nd–Sr isotopic compositions are close to the evolved basalts (Li et al., 2002).

Samples XG-12, XG-14 and 4009 are anomalous. XG-12 and XG-14 are amygdaloid-bearing basalts,

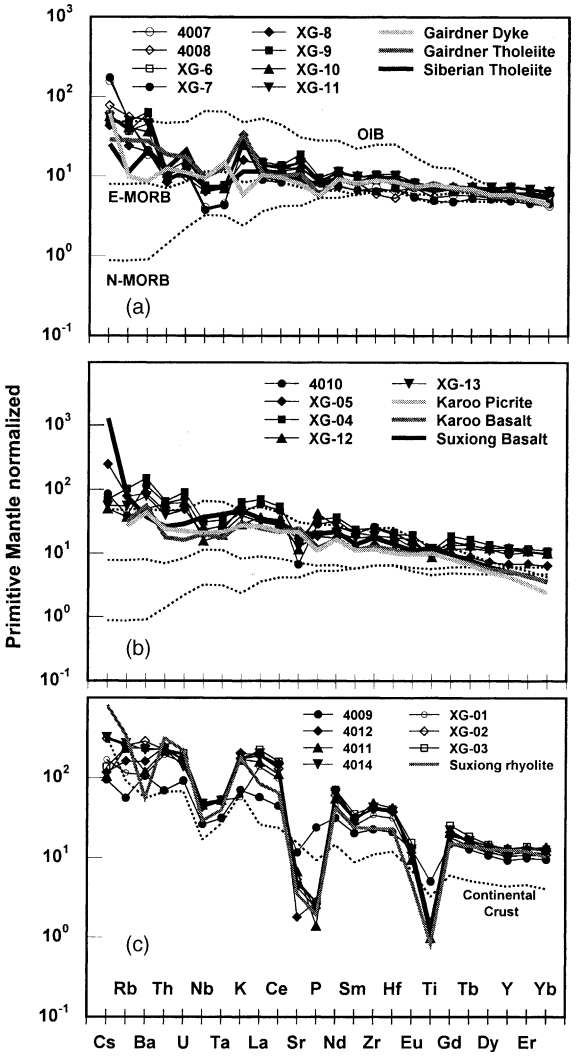

Fig. 10. Primitive mantle-normalized incompatible trace element distributions for the Tiechuanshan tholeiites (a), alkaline basalts (b), and rhyolites (c). Primitive mantle values are from Sun and McDonough (1989). For comparison, compositions of N-MORB, E-MORB, OIB (Sun and McDonough, 1989) are shown as dot lines in (a) and (b) and the continental crust (Rudnick and Fountain, 1995) in (c). Also shown are the Gairdner Dyke (Zhao et al., 1994) and Siberian (Hawkesworth et al., 1995) tholeiites in (a), the Karoo picrite and basalt (Gibson et al., 2000) and the Suxiong alkaline basalt (Li et al., 2002) in (b), and Suxiong rhyolite (Li et al., 2002) in (c).

in which the trapped felsic magma might account for their anomalously high SiO_2 and LREE and low Eu/Eu* and ε_{Nd} (t) values (+3.8 and +1.4, respectively). Sample 4009 may represent a mixture between

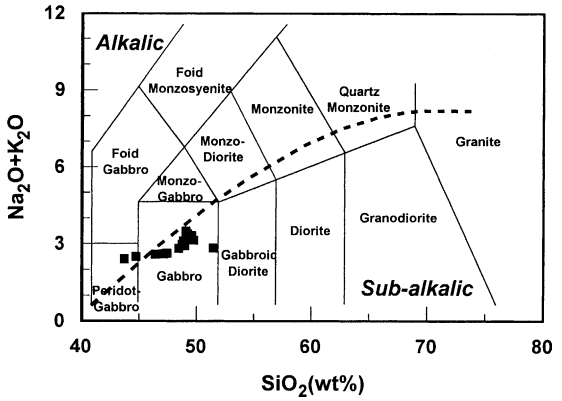

Fig. 11. $Na_2O + K_2O$ vs. SiO_2 plot (Middlemost, 1994) plot for Wangjiangshan Gabbros.

basaltic and felsic magmas as inferred from its high SiO_2 and initial $^{87}Sr/^{86}Sr$ ratio (0.7073) and trace element composition similar to the other Tiechuanshan felsic rocks but with low REE concentration and positive ε_{Nd} (+3.0).

5.3. Wangjiangshan Gabbro

The Wangjiangshan Gabbros fall into the subalkalic gabbro field in Fig. 11 and display a tholeiitic trend (Fig. 12). In the spider diagram, they are depleted in Cs, Rb, Th, Nb, Ta, Zr and Hf and enriched in Sr and Ba (Fig. 13) together with positive Eu anomalies ($Eu/Eu^* = 1.21–2.18$), which points to an important role of plagioclase accumulation. Depletion in LILE (Cs, Rb, Th and U), Zr and Hf discriminates the Wangjiangshan Gabbros from mafic plutons from the Siberian Trap (Hawkesworth et al., 1995) and Gairdner Dyke (Zhao et al., 1994). Compared with the Tiechuanshan tholeiites, these Gabbros display a wider SiO_2 range from 43 to 51 wt.%. The less fractionated samples 2KW-25, -26, -22 and -32 with low SiO_2 (<49 wt.%) and high MgO (8–9 wt.%) also have higher Ni and Cr concentrations compared to samples with SiO_2 ≥49 wt.% and MgO ≤8 wt.% (Table 4; Fig. 13). In addition, most of the samples except WJS-3 and WJS-6 show clear co-variations of TiO_2, Na_2O, CaO, MgO and Ni with SiO_2 (Fig. 14). WJS-1 and WJS-2 have significantly lower ε_{Nd} (820 Ma) and therefore implies involvement of crustal component. Although WJS-3 and WJS-6 also show low ε_{Nd} (t), their low SiO_2 and high CaO and TiO_2 character is

Table 4
Chemical compositions of the Wangjiangshan Gabbro

Sample	KW-19	KW-20	KW-21	KW-22	KW-23	KW-24	KW-25	KW-26	KW-27	KW-28
In wt.%										
SiO_2	49.25	48.84	48.73	47.11	49.56	48.96	46.37	46.38	51.43	49.21
TiO_2	1.14	1.08	0.92	1.38	1.08	0.91	1.93	3.26	0.78	1.31
Al_2O_3	18.83	17.89	17.52	17.06	18.78	17.20	16.25	14.46	18.49	18.26
Fe_2O_{3t}	9.96	10.71	10.88	11.95	9.16	11.08	12.89	13.99	8.16	10.14
Fe_2O_3	nd	nd	nd	nd	nd	nd	nd	nd	nd	nd
FeO	6.80	7.72	9.70	8.85	6.42	8.60	9.40	9.82	5.55	6.90
MnO	0.13	0.15	0.18	0.16	0.14	0.18	0.18	0.20	0.17	0.14
MgO	6.61	7.72	7.93	9.34	6.92	8.22	9.12	8.96	7.34	6.62
CaO	10.42	10.17	10.39	10.44	10.48	10.53	10.39	9.92	11.28	10.40
Na_2O	2.93	2.84	2.77	2.43	3.02	2.72	2.42	2.34	2.67	3.01
K_2O	0.36	0.27	0.21	0.18	0.30	0.21	0.18	0.26	0.17	0.37
P_2O_5	0.21	0.15	0.25	0.03	0.16	0.15	0.32	0.32	0.15	0.10
CO_2	nd	nd	nd	nd	nd	nd	nd	nd	nd	nd
H_2O^+	nd	nd	nd	nd	nd	nd	nd	nd	nd	nd
LOI	0.06	0.11	0.22	0.30	0.11	0.19	0.07	0.32	0.06	0.09
Total	99.90	99.93	100.00	100.38	99.71	100.35	100.12	100.41	100.70	99.65
Mg numbers	62	64	64	66	65	65	64	61	69	62
In ppm										
Cr	160	132	301	346	169	313	354	312	288	167
Ni	81.2	176	173	198	53.3	163	202	193	73.5	63.6
Rb	7.68	4.43	2.29	1.49	3.93	1.81	1.31	5.49	1.30	7.46
Sr	406	381	335	282	400	316	275	243	624	397
Y	13.6	11.9	16.2	11.0	12.1	14.6	19.2	22.9	11.4	13.8
Zr	42.9	34.9	32.6	36.3	40.6	32.7	48.8	99.5	20.6	42.5
Nb	2.60	1.95	1.69	2.04	2.6	1.54	3.69	7.43	0.79	2.29
Cs	0.19	0.15	0.22	0.04	0.17	0.21	0.04	0.15	0.08	0.23
Ba	126	111	181	137	121	178	149	165	112	128
La	5.68	4.49	5.05	2.55	5.00	4.25	5.55	6.30	2.74	4.69
Ce	13.1	10.5	12.4	5.97	11.5	10.4	14.8	16.6	6.80	11.2
Pr	1.84	1.47	1.88	0.89	1.54	1.50	2.19	2.46	1.04	1.55
Nd	8.36	6.78	9.32	4.71	7.30	7.80	11.1	12.7	5.12	7.36
Sm	2.16	1.87	2.73	1.37	2.04	2.24	3.10	3.55	1.67	2.04
Eu	1.02	0.95	1.59	1.03	0.95	1.56	1.50	1.52	1.17	1.03
Gd	2.04	1.74	2.49	1.50	1.84	2.15	2.93	3.25	1.62	1.84
Tb	0.36	0.30	0.44	0.27	0.32	0.39	0.54	0.62	0.30	0.35
Dy	2.36	2.07	2.87	2.01	2.11	2.55	3.32	4.25	1.96	2.48
Ho	0.50	0.40	0.59	0.43	0.45	0.58	0.73	0.95	0.44	0.54
Er	1.39	1.12	1.61	1.15	1.18	1.47	1.90	2.32	1.14	1.49
Tm	0.20	0.17	0.22	0.16	0.17	0.22	0.26	0.33	0.16	0.19
Yb	1.29	1.12	1.50	1.14	1.11	1.45	1.64	2.32	1.11	1.43
Lu	0.19	0.16	0.22	0.17	0.17	0.20	0.26	0.33	0.15	0.22
Hf	1.20	0.94	0.87	1.01	1.12	0.89	1.35	2.52	0.59	1.23
Ta	0.19	0.15	0.13	0.15	0.17	0.11	0.28	0.57	0.06	0.16
Th	0.83	0.34	0.14	0.06	0.43	0.09	0.11	0.29	0.08	0.35
U	0.18	0.09	0.05	0.02	0.14	0.03	0.04	0.10	0.03	0.11

Table 4 (*Continued*)

	KW-29	KW-30	KW-31	KW-32	KW-34	WJS-1	WJS-2	WJS-3	WJS-4	WJS-6
In wt.%										
SiO_2	47.39	49.17	50.30	47.38	50.22	48.61	49.30	44.34	47.87	43.32
TiO_2	1.56	1.38	1.00	1.56	1.00	1.50	1.47	1.99	1.38	2.93
Al_2O_3	16.53	18.16	18.25	16.39	18.49	18.51	17.43	16.12	17.01	15.75
Fe_2O_{3t}	12.68	10.94	8.95	12.74	8.72	nd	nd	nd	nd	nd
Fe_2O_3	nd	nd	nd	nd	nd	2.93	2.10	6.98	2.48	6.82
FeO	8.95	6.90	5.80	8.95	5.62	7.08	7.75	9.28	8.32	10.02
MnO	0.18	0.16	0.15	0.18	0.15	0.14	0.16	0.15	0.19	0.15
MgO	8.96	6.51	6.94	9.14	6.82	5.16	6.88	6.07	8.07	5.81
CaO	9.98	10.19	11.09	9.99	11.10	11.59	10.87	11.68	10.42	11.85
Na_2O	2.46	2.84	2.80	2.38	2.87	2.99	2.87	2.25	2.61	2.19
K_2O	0.18	0.23	0.19	0.17	0.19	0.26	0.25	0.24	0.19	0.21
P_2O_5	0.05	0.19	0.07	0.04	0.09	0.37	0.06	0.09	0.30	0.11
CO_2	nd	nd	nd	nd	nd	0.09	0.09	0.04	0.06	0.04
H_2O^+	nd	nd	nd	nd	nd	0.56	0.57	0.55	0.89	0.56
LOI	0.27	0.03	0.06	0.35	0.07	nd	nd	nd	nd	nd
Total	100.24	99.80	99.80	100.32	99.72	99.79	99.80	99.78	99.79	99.76
Mg numbers	64	60	66	64	66	54	61	47	63	44
In ppm										
Cr	368	21.2	277	355	261	215	246	9.9	186	11.6
Ni	186	57.4	47.2	191	38.3	72.4	73.1	21.6	108	10.5
Rb	1.24	2.24	1.31	1.30	1.58	2.33	2.68	2.63	1.58	3.72
Sr	273	623	631	280	643	404	372	443	393	395
Y	13.3	13.2	11.9	13.6	12.0	16.3	11.8	12.6	20.6	13.6
Zr	39.9	31.7	22.7	43.9	24	33.7	41.0	38.9	43.8	37.6
Nb	2.21	1.52	1.00	2.42	0.99	1.64	2.80	1.99	3.48	1.70
Cs	0.05	0.12	0.05	0.05	0.04	0.10	0.11	0.08	0.12	0.14
Ba	141	149	109	150	114	191	192	145	170	137
La	3.22	3.69	2.74	3.17	2.93	7.17	4.13	4.88	9.54	3.86
Ce	7.76	8.84	6.84	7.66	7.06	17.47	9.48	11.6	22.7	9.67
Pr	1.14	1.28	1.05	1.16	1.06	2.31	1.22	1.54	2.94	1.34
Nd	5.82	6.06	5.16	5.95	5.38	11.7	6.22	7.68	14.5	7.12
Sm	1.86	1.94	1.66	1.81	1.66	2.92	1.70	2.06	3.58	2.07
Eu	1.20	1.30	1.05	1.26	1.10	1.71	1.44	0.91	1.62	1.17
Gd	1.77	1.89	1.73	1.86	1.76	3.60	2.21	2.53	4.27	2.76
Tb	0.34	0.34	0.30	0.36	0.32	0.53	0.35	0.40	0.67	0.43
Dy	2.31	2.27	2.22	2.50	1.99	3.04	2.10	2.24	3.80	2.51
Ho	0.53	0.54	0.48	0.55	0.47	0.65	0.47	0.49	0.83	0.55
Er	1.46	1.34	1.27	1.48	1.24	1.69	1.28	1.31	2.26	1.43
Tm	0.20	0.20	0.19	0.23	0.17	0.24	0.20	0.20	0.33	0.20
Yb	1.39	1.50	1.32	1.44	1.21	1.36	1.18	1.10	1.89	1.20
Lu	0.23	0.20	0.21	0.23	0.18	0.19	0.17	0.16	0.28	0.17
Hf	1.06	0.87	0.72	1.20	0.72	1.05	1.23	1.17	1.46	1.21
Ta	0.18	0.12	0.08	0.19	0.08	0.11	0.18	0.13	0.21	0.13
Th	0.07	0.12	0.07	0.05	0.10	0.35	0.24	0.31	0.26	0.39
U	0.03	0.04	0.02	0.02	0.03	0.09	0.07	0.06	0.06	0.09

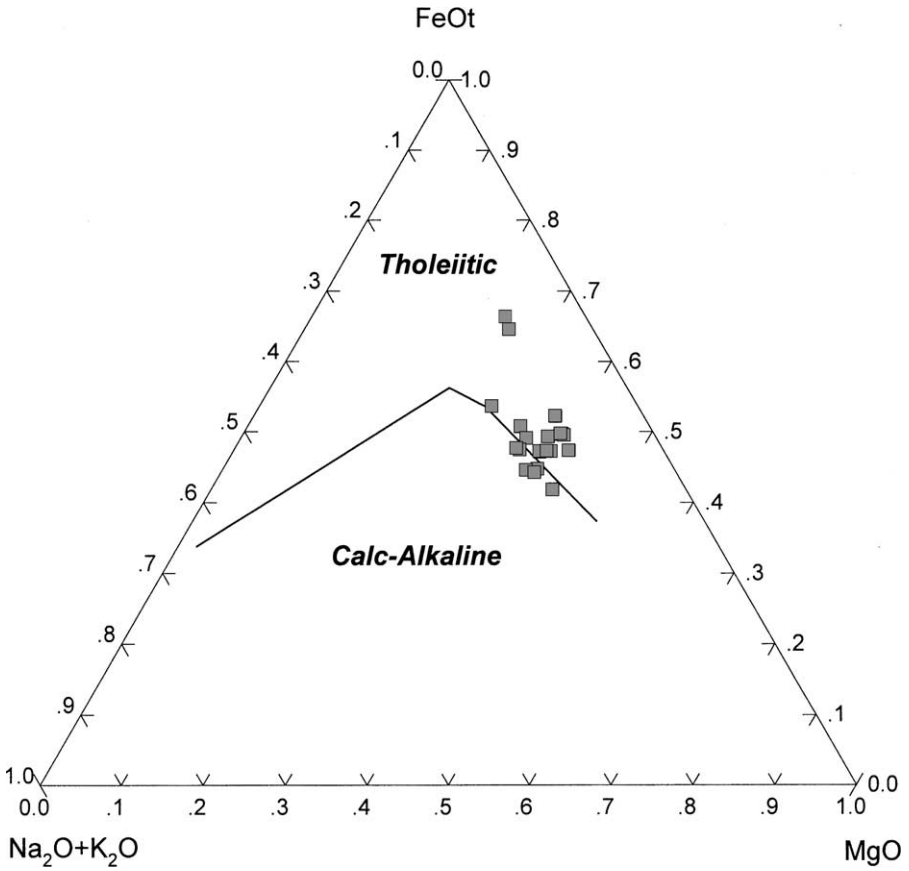

Fig. 12. $Na_2O + K_2O$–FeO_{total}–MgO triangle plot for Wangjiangshan Gabbros, which show a tholeiitic trend.

different form that of WJS-1 and WJS-2. The high CaO cannot be explained by involvement of carbonate because of their low CO_2 (0.04 wt.%). Further studies are required on resolving the combined low ε_{Nd} (t) and low SiO_2 character of WJS-3 and WJS-6. Apart from these four samples, the other samples with high ε_{Nd} (t) show no correlation between ε_{Nd} (t) and SiO_2 (Fig. 14f). The above evidence suggests that the high ε_{Nd} (t) samples are co-magmatic without significant crustal contamination.

6. Petrogenesis

6.1. Xixiang volcanic rocks

As mentioned above, geochemical and Nd isotopic distinctions are evident between the boninitic and low-Ti tholeiitic associations from the lower Xixiang Group and the LILE-enriched basaltic and andesitic suite from the upper Xixiang Group. The diversities infer differences in source composition and/or petrogenesis. The combined high Mg number, Cr and Ni of the lower Xixiang mafic rocks imply derivation from magma with insignificant fractionation of olivine and pyroxene (Shinjo, 1999). Depletion in Nb and Ta suggests involvement of a crustal or slab-related component. However, their high ε_{Nd} (t) values similar to the upper limit of contemporary depleted mantle rule out a significant role of crustal and/or slab component(s). The Xixiang high-Mg andesites may be classified into Type 2 low-Ca boninite of Crawford et al. (1989), which is expected to be derived from melting of a refractory peridotite source at ~8–15 kbar and 1100–1150 °C. Combination of the LREE-depleted rare earth element pattern, low incompatible element

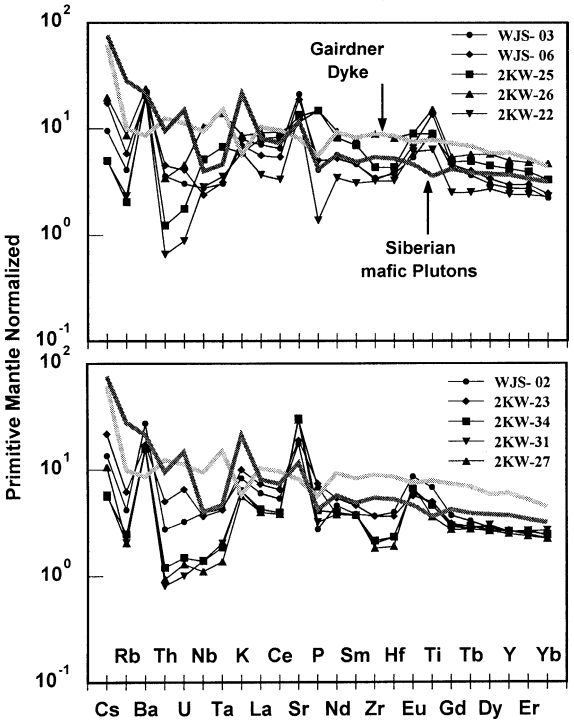

Fig. 13. Primitive mantle-normalized incompatible trace element distributions for Wangjiangshan Gabbros with SiO_2<49% and MgO 8–9% (a) and SiO_2>49% and MgO<8% (b). Primitive mantle values are from Sun and McDonough (1989). Data for average Gairdner Dyke and Siberian mafic pluton are from Zhao et al. (1994) and Hawkesworth et al. (1995), respectively.

(including K_2O) concentrations and high ε_{Nd} (t) values of the Xixiang boninites and low-Ti tholeiites suggest a derivation from a time-integrated depleted mantle source.

Two-stage models are advocated to interpret the genesis of boninites or high-Mg andesites, where previously depleted peridotite is fluxed by hydrous fluid or melt from dehydration of a subducted slab or by partial melt derived from an OIB-type source mantle (Crawford et al., 1989). Interaction between ascending melts originated from slab melting and mantle wedge is proposed to account for the generation of high-Mg andesites and adakites in relation to subduction of oceanic crust (e.g. Yogodzinski et al., 1995; Stern and Kilian, 1996; Shinjo, 1999). Low Al_2O_3 and La_N/Yb_N and absence of positive Sr anomalies negate dominance of a slab component in the Xixiang boninitic and high-Mg andesitic magma. This is also supported by depletion of LILE.

It is well known that high temperatures and/or the existence of fluids are critical for melting a refractory peridotite (e.g. Crawford et al., 1989). The convergent margin–plume interaction setting offers such an environment (Brown and Jenner, 1989) and is used to explain volcanic rocks from the Abitibi belt (Fan and Kerrich, 1997; Kerrich et al., 1998; Wyman, 1999) and the Koh ophiolite (Meffre et al., 1996). This model is also applied to a mantle wedge setting, where refractory peridotite had experienced an OIB-type enrichment event prior to subduction and is followed by the modification of hydrous fluids derived from subducted slab (Beccaluva and Serri, 1988; Hickey-Vargas and Reagan, 1987). Such a model can explain close association of boninitic, high-Mg tholeiitic and other subduction-related lavas in a fore-arc setting. Therefore, the lower Xixiang volcanic rocks probably formed in a fore-arc environment.

The upper Xixiang volcanic rocks, regardless of rock type, show enrichment in LILE, Zr and Hf with fractionated LREE and variable degrees of negative Eu anomalies. They display clear arc signatures of depletion in Nb, Ta, Ti and Eu. The similarities between the mafic and felsic lavas in trace element distribution (Fig. 6a and b) and positive ε_{Nd} (t) reveal that they were co-magmatic. An AFC process may explain the relatively lower ε_{Nd} (t) of the felsic rocks. It should be noted that dacite and rhyolite samples 5002, 5006, SGH-2, 5208, 5211 and 5220 from the upper Xixiang Group are highly alkaline, resembling intra-plate granite (Pearce et al., 1984). Alkaline rocks are not uncommon in a back-arc setting (Foley and Peccerillo, 1992; Turner et al., 1996), so, the occurrence of the Xixiang alkaline rhyolites may point to the development of a back-arc setting.

6.2. Tiechuanshan volcanic suite

6.2.1. Basalt

Negative Nb and Ta anomalies suggest involvement of crustal or subcontinental lithosphere mantle (SCLM) components in the Tiechuanshan tholeiites. However, their consistently high ε_{Nd} (817 Ma) values (+4.6 to +5.3) and low initial $^{87}Sr/^{86}Sr$ ratios (0.7040–0.7049) for all the tholeiites with variable

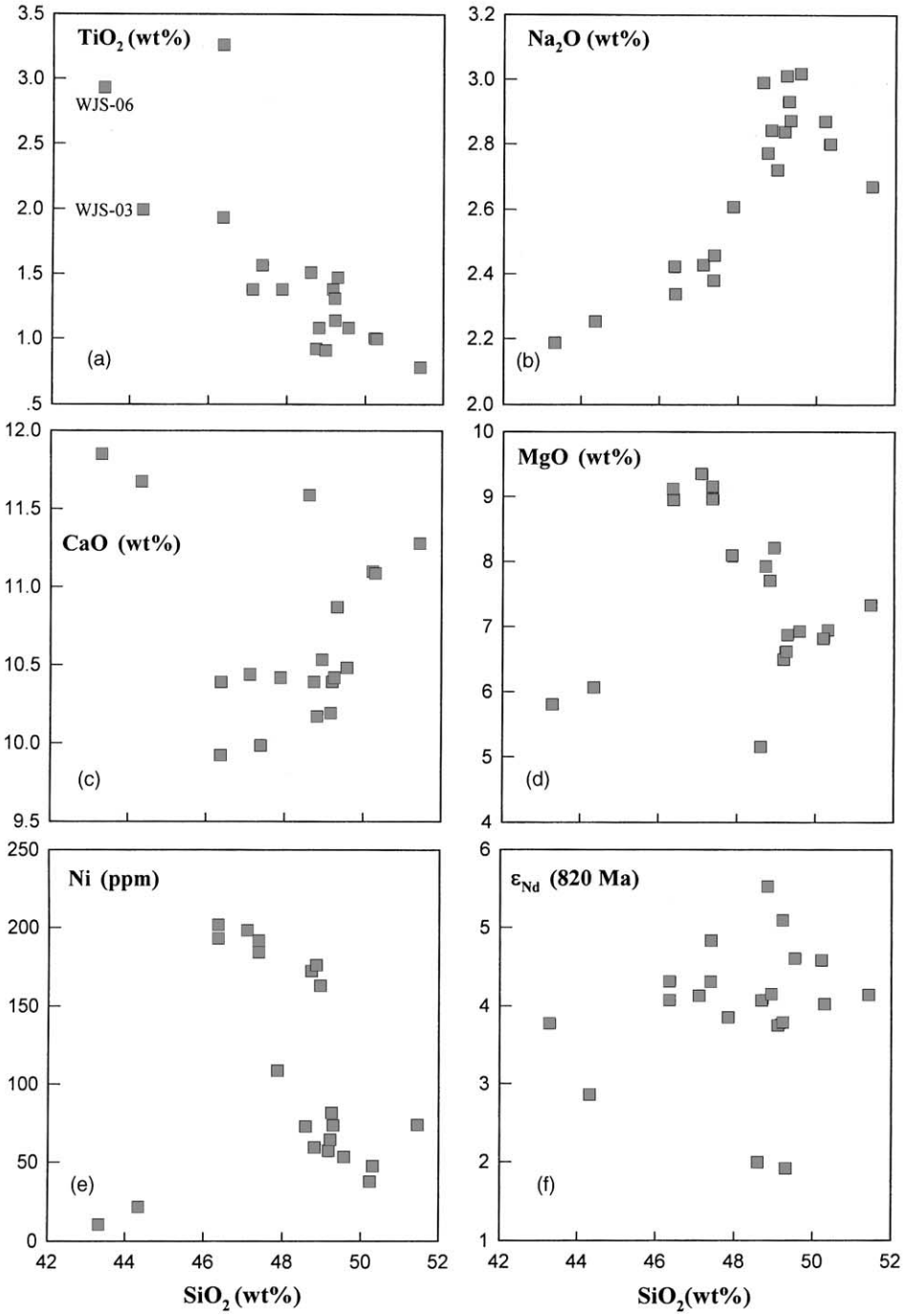

Fig. 14. Variations of TiO_2, Na_2O, CaO, MgO, Ni and ε_{Nd} (820 Ma) with SiO_2 for Wangjiangshan Gabbros.

Table 5
Sm–Nd and Rb–Sr isotopic compositions of the Xixiang Group

Sample	$^{143}Nd/^{144}Nd$	$2\sigma_m$	Nd	Sm	$^{147}Sm/^{144}Nd$	$^{87}Sr/^{86}Sr$	$2\sigma_m$	$^{87}Rb/^{86}Sr$	Sr	Rb	T_{DM} (Ga)	ε_{Nd} (t)
Upper Xixiang Group												
5002	0.512356	5	26.71	5.178	0.1172	0.731743	45	2.116	198	144	1.25	3.6
5006	0.512367	7	21.48	4.073	0.1146	0.726085	43	2.098	158	115	1.20	4.1
5008	0.512525	5	20.74	4.739	0.1381	0.706188	45	0.238	359	29.5	1.26	4.5
5109	0.512548	8	17.40	3.950	0.1373	0.722285	33	1.721	153	90.6	1.20	5.1
5112	0.512400	5	23.50	5.404	0.1390	0.712360	48	0.952	139	45.8	1.53	2.0
5201	0.512866	5	16.18	4.722	0.1765	0.709263	35	0.462	350	55.8	1.16	6.8
5204	0.512404	5	35.03	7.104	0.1226	0.709360	31	0.470	386	62.7	1.25	3.9
5208	0.512575	5	54.83	13.28	0.1464	0.764902	65	5.955	43.0	88.0	1.30	4.6
5211	0.512572	5	40.35	10.01	0.1500	0.804765	33	9.183	36.7	116	1.38	4.1
5212	0.512491	5	31.43	6.493	0.1249	0.704959	24	0.100	774	26.7	1.13	5.4
5215	0.512372	5	30.25	6.158	0.1231	0.709754	25	0.489	414	69.9	1.31	3.3
5216	0.512370	6	30.59	6.374	0.1260	0.715209	18	1.042	192	69.1	1.35	2.9
5220	0.512447	7	37.80	9.016	0.1442	0.724965	29	2.436	101	84.6	1.54	2.3
SGH-1	0.512435	5	24.62	5.010	0.1230	0.706791	17	0.253	370	32.3	1.20	4.5
SGH-2	0.512595	4	54.18	12.56	0.1401	0.731525	54	2.725	96.5	90.6	1.15	5.7
Lower Xixiang Group												
5408	0.513059	7	4.026	1.431	0.2149	0.704393	26	0.009	369	1.10	−12.2	6.0
5410	0.513192	7	2.960	1.143	0.2336	0.705791	36	0.067	185	4.28	0.32	6.3
5413	0.512997	6	8.724	2.863	0.1984	0.706679	40	0.225	87.6	6.82	1.52	6.8
5414	0.513058	5	10.59	3.360	0.1918	0.704513	19	0.078	139	3.73	0.64	8.8
5415	0.512458	6	17.08	3.524	0.1248	0.709325	23	0.535	246	45.5	1.19	5.3
5416	0.512481	9	19.23	4.409	0.1386	0.729211	27	2.415	108	90.0	1.36	4.0
5503	0.512708	5	19.59	5.173	0.1597	0.704247	20	0.036	228	2.85	1.25	5.9
5509	0.512666	5	17.52	4.650	0.1605	0.733602	33	2.782	58.0	55.6	1.38	5.0
5516	0.512664	5	19.24	4.959	0.1558	0.705101	33	0.155	215	11.5	1.28	5.5
5519	0.512533	8	9.049	2.076	0.1387	0.703815	21	0.032	638	6.99	1.25	5.0
5520	0.512519	5	11.78	2.567	0.1318	0.706398	19	0.271	438	41.0	1.17	5.6
BMX-1	0.512398	5	17.26	3.440	0.1205	0.703519	26	0.046	3085	49.2	1.23	4.6
BMX-2	0.512447	8	8.995	2.032	0.1366	0.709246	39	0.654	66.4	15.0	1.39	3.6

Data of $^{144}Nd/^{143}Nd$ and $^{87}Sr/^{86}Sr$ are measured ratio, $2\sigma_m$ denotes mean standard deviation reported at 2σ value $\times 10^{-6}$. The decay constant (λ) of ^{147}Sm used in model age calculation is 0.00654 Ga^{-1}. The depleted mantle model age (T_{DM}) assumes a linear evolution of isotopic composition from ε_{Nd} (t) = 0 at 4.56 Ga to approximately +10 at the present time. The notation of ε_{Nd} follows DePaolo and Wasserburg (1976), and the model age (T_{DM}) is calculated using equation: $T_{DM} = 1/\lambda \times \ln\{1+[(^{143}Nd/^{144}Nd)_{sample} - 0.51315]/[(^{147}Sm/^{144}Nd)_{sample} - 0.2137]\}$. $^{143}Nd/^{144}Nd$ (CHUR) = 0.512638 and $^{147}Sm/^{144}Nd$ (CHUR) = 0.1967 are used in the calculation of the ε value, where t = 950, 897, 817 and 820 Ma are adopted for the lower and upper units of the Xixiang Group, the Tiechuanshan Formation, and the Wangjiangshan Gabbros in this table and Tables 6 and 7, respectively (see text for explanation).

SiO_2 and Nb/La ratio (0.42–0.59) suggest an insignificant crustal contamination.

High Mg number and compatible elemental contents, coupled with high positive ε_{Nd} (t) and low REE and La_N/Yb_N ratio, imply that the Tiechuanshan tholeiites were derived from a time-integrated depleted mantle source. Tholeiites with similar geochemical and isotopic compositions characterize continental rift volcanic suites from Siberia, Karoo, Deccan and southeastern Australia (Campbell and Griffiths, 1990; Zhao et al., 1994; Hawkesworth et al., 1995; Arndt et al., 1998; Gibson et al., 2000) (Fig. 10a). Despite controversy on the role of SCLM in the genesis of continental tholeiites, it is generally agreed that the tholeiitic parental magma has a plume-related derivation (McKenzie and Bickle, 1988; Arndt and Christensen, 1992; Gallagher and Hawkersworth, 1992; Arndt et al., 1998). Hawkesworth et al. (1995) and Barrat et al. (1998) advocate that multiple MORB, OIB and SCLM sources are needed to account for the geochemical and isotopic compositions of igneous associations from continental rifts and continental flood

basalt (CFB) provinces. A dominant time-integrated depleted mantle may explain the coupled high positive ε_{Nd} (t) value, low initial $^{87}Sr/^{86}Sr$ ratio and low TiO_2, LILE and LREE contents of the Tiechuanshan tholeiites.

For a given SiO_2 content, the Tiechuanshan alkaline basalts have significantly lower Mg numbers (46–17), Cr (43–5.0 ppm) and Ni (33–4.5 ppm) concentrations compared to the intercalated tholeiitic basalts. Negative Sr and Eu ($Eu/Eu^* = 0.81–1.0$) anomalies suggest plagioclase fractionation for the alkaline basalt (Fig. 10b). Therefore, the alkaline basalt is more evolved. Variable ε_{Nd} (t) values (+0.2 to +3.9) and initial $^{87}Sr/^{86}Sr$ ratio (0.7030–0.7051) as well as negative Nb and Ta anomalies also suggest the role of an AFC process. However, the less evolved alkaline basalts with low SiO_2 (XG-4 and XG-13) correspond to high TiO_2 (2.59–2.45 wt.%) and ε_{Nd} (t) values (+2.5 and +3.0) which are very similar to the primitive Suxiong alkaline basalts from the Kangdian Rift (Li et al., 2002). These rocks are also characterized by high K_2O (XG-4 even has a normative nepheline) and TiO_2 contents (2.16–2.59 wt.%). High-Ti (>1.3 wt.%) basalts are often found in extension settings (e.g. back-arc or intra-continental rifts; Allen, 2000), and have a deep mantle origin via low degrees of partial melting (Campbell and Griffiths, 1990; Albarède, 1992; Arndt et al., 1998). Nepheline-bearing alkaline basalts are considered to be generated at the depths of 50–70 km in lithospheric thinning settings during the continental extension (e.g. DePaolo and Daley, 2000). The similar isotopic and geochemical compositions between the Tiechuanshan alkaline and high-Ti basalts and worldwide continental rift basalts and CFB suites suggest a similar OIB-type or plume-related petrogenesis (Fig. 10b).

6.2.2. Dacite–rhyolite

The Tiechuanshan dacites and rhyolites are highly alkaline with Na_2O 3.47–4.84 and K_2O 1.72–6.12 wt.%. They fall into the fields of within-plate or A-type granites on the Ga/Al versus Zr diagram (Pearce et al., 1984) and the Nb–Y–Ce triangle plot (Whalen et al., 1987) (not shown). Negative ε_{Nd} (t) values (−2.5 to −4.9), high and variable initial $^{87}Sr/^{86}Sr$ ratios (0.7054–0.7106) and pronounced Nb, Ta, Eu, P and Ti depletions imply a dominant crustal origin (Fig. 10c). In addition, the felsic rocks are weakly peraluminous with molecular $Al_2O_3/(CaO + Na_2O + K_2O)$ ratio = 0.97–1.12. Petrogenesis of A-type granitoid magma from simple anatexis within a stable continental setting with a normal geotherm is not supported by available evidence (e.g. Bonin, 1996). Additional heat source and deep mantle-derived melts are proposed to generate the A-type granitoids (Montel and Vielzeuf, 1997; Mingram et al., 2000). Accordingly, crustal anatexis facilitated by plume-related heating and fluid fluxing is invoked to account for the genesis of the Tiechuanshan dacites and rhyolites. The Tiechuanshan volcanic suites may have formed in an intra-continental rift setting, similar to the bimodal alkaline magmatism formed in continental rift (e.g. Davies and Macdonald, 1987; Wilson, 1989).

As discussed above, the upper Xixiang Group is only slightly younger than the lower Xixiang Group. However, both of them are ~80 Ma older than the Tiechuanshan bimodal volcanic suite. Such an age gap suggests that the Tiechuanshan Formation and Xixiang Group were formed in different tectonic settings, although the upper Xixiang and Tiechuanshan felsic volcanic rocks show similar major and trace element compositions. This inference is supported by the contrasting positive (+2.3 to +5.7) versus negative (−2.5 to −4.9) ε_{Nd} values for the upper Xixiang and Tiechuanshan felsic volcanic rocks, respectively.

6.3. Wangjiangshan Gabbro

As discussed above, the Wangjiangshan Gabbros with high ε_{Nd} (t) were formed without significant crustal contributions. Although they have essentially identical ε_{Nd} (t) values (+5.5 to +3.8) to the coeval southeastern Australian Gairdner Dyke (+4.3 to +3.5; Zhao et al., 1994), their MgO (9.34–8.96 wt.%), Cr (368–312 ppm) and Ni (201–185 ppm) contents are remarkably higher than the Gairdner Dyke (MgO 7.55–4.57 wt.%, Cr 200–60 ppm and Ni 140–66 ppm; Zhao et al., 1994). This is coupled by considerably lower incompatible element contents, especially Rb, U, and Th with moderate enrichment in Ti for the Wangjiangshan Gabbros (Fig. 14). These geochemical and isotopic features can be interpreted in terms of higher degree of partial melting of the source mantle for the Wangjiangshan Gabbros. This in turn implies a higher geotherm for the formation

of the Wangjiangshan Gabbro relative to the Gairdner Dyke.

7. Tectonic implications

The Grenvillian (~1.3–1.0 Ga) orogenic belts are regarded as one of critical links to individual continents in the configuration of Rodinia (e.g. Dalziel, 1991; Hoffman, 1991; Moores, 1991; Keppie et al., 2001), although local younger collision events are also proposed (Vance et al., 1998). However, constraints on the Grenvillian orogeny in South China are limited due partly to widespread thick Phanerozoic sedimentary rocks covering the Precambrian basements and partly to the late Paleozoic to early Mesozoic tectonic reworking along the South China margins. It is argued that the Neoproterozoic collision between the Yangtze craton and the Cathaysia block resulted in the unification of South China, as indicated by occurrences of arc igneous suites with age of ca. 1000–970 Ma along their connection boundary (e.g. Chen et al., 1991; Li et al., 1994, 1997; Li and McCulloch, 1996). Neoproterozoic mafic-ultramafic dykes and granitic plutons occurred in the Guangxi province along southern margin of Yangtze craton were dated at 828 ± 7 and 819 ± 9 to 826 ± 10 Ma, respectively, and have been interpreted to be co-magmatic and plume-related in petrogenesis (Li et al., 1999). The consistency in age and chemical and isotopic compositions between the Neoproterozoic igneous suites in/around the Yangtze carton and southeastern Australia (Zhao et al., 1994; Wingate et al., 1998) suggest a genetic link between them. Distribution of the Neoproterozoic arc volcanic rocks along margins of the Yangtze craton can thus be used to delineate location of its collision with neighboring continents under the overall context of Rodinia.

The 950–897 Ma Xixiang arc suites show subduction and amalgamation of tectonic blocks along the northwestern margin of the Yangtze craton during the early Neoproterozoic, although timing of the events is somewhat younger than the Grenvillian orogeny. The younger Tiechuanshan bimodal volcanic suite and the Wangjiangshan Gabbro were formed in an intra-continental rift setting which is distinct from the upper Xixiang unit. The age gap between the upper

Table 6
Sm–Nd and Rb–Sr isotopic compositions of the Tiechuanshan Formation

Sample	$^{143}Nd/^{144}Nd$	$2\sigma_m$	Nd	Sm	$^{147}Sm/^{144}Nd$	$^{87}Sr/^{86}Sr$	$2\sigma_m$	$^{87}Rb/^{86}Sr$	Sr	Rb	T_{DM} (Ga)	ε_{Nd} (*t*)
XG-1	0.511965	5	63.01	10.18	0.0976	0.733541	73	2.400	92.6	76.6	1.55	−2.8
XG-2	0.511904	5	84.22	11.69	0.0839	0.750056	30	3.470	109	130	1.46	−2.5
XG-3	0.511881	7	99.79	15.30	0.0926	0.755261	45	3.887	92.1	123	1.59	−3.9
XG-4	0.512396	5	49.31	10.43	0.1278	0.708358	15	0.460	337	53.7	1.34	2.5
XG-5	0.512314	5	27.080	6.023	0.1345	0.709022	19	0.331	444	50.8	1.61	0.2
XG-6	0.512703	6	14.54	3.822	0.1589	0.706924	15	0.172	360	21.4	1.24	5.2
XG-7	0.512765	4	10.87	3.087	0.1717	0.708861	12	0.425	215	31.6	1.39	5.1
XG-8	0.512715	4	15.60	4.292	0.1663	0.706331	10	0.134	320	14.7	1.40	4.7
XG-9	0.512713	5	16.72	4.570	0.1652	0.707154	12	0.226	379	29.6	1.37	4.8
XG-10	0.512727	4	15.37	4.307	0.1694	0.707179	12	0.274	261	24.7	1.45	4.6
XG-11	0.512729	4	16.42	4.536	0.1671	0.706924	12	0.229	286	22.6	1.37	4.9
XG-12	0.512591	4	36.77	9.200	0.1513	0.707151	10	0.280	245	23.7	1.36	3.8
XG-13	0.512495	4	30.46	7.120	0.1413	0.709305	11	0.404	253	35.3	1.38	3.0
XG-14	0.512328	4	104.2	21.62	0.1254	0.710201	10	0.420	240	34.9	1.42	1.4
4007	0.512731	5	10.20	2.846	0.1687	0.707938	19	0.248	259	22.2	1.42	4.8
4008	0.512734	6	14.39	4.055	0.1704	0.707544	14	0.294	272	27.7	1.46	4.6
4009	0.512442	4	40.57	8.802	0.1312	0.712162	17	0.415	246	35.3	1.31	3.0
4010	0.512350	4	41.61	8.873	0.1289	0.710569	22	0.516	140	24.9	1.44	1.5
4011	0.511948	6	74.90	12.95	0.1045	0.740008	45	2.801	132	128	1.67	−3.8
4012	0.511869	4	96.59	14.44	0.0903	0.795298	34	7.390	39.0	98.7	1.58	−3.9
4014	0.511888	4	87.41	14.39	0.0995	0.764748	66	4.614	86.6	137	1.68	−4.5
4015	0.511968	4	53.52	10.53	0.1189	0.836236	25	10.94	14.1	52.7	1.90	−4.9

Table 7
Sm–Nd isotopic composition of the Wangjiangshan Gabbro

Sample	$^{143}Nd/^{144}Nd$	$2\sigma_m$	Nd	Sm	$^{147}Sm/^{144}Nd$	T_{DM} (Ga)	ε_{Nd} (t)
KW-19	0.512615	8	8.346	2.157	0.1563	1.42	3.8
KW-20	0.512717	6	6.928	1.820	0.1588	1.20	5.5
KW-21	0.512664	5	10.13	2.727	0.1627	1.45	4.1
KW-22	0.512787	5	4.728	1.446	0.1850	1.92	4.1
KW-23	0.512657	5	7.689	1.989	0.1564	1.31	4.6
KW-24	0.512701	5	8.076	2.256	0.1689	1.52	4.2
KW-25	0.512687	5	11.52	3.181	0.1670	1.51	4.1
KW-26	0.512706	6	12.89	3.587	0.1683	1.49	4.3
KW-27	0.512759	4	5.399	1.606	0.1798	1.76	4.1
KW-28	0.512724	5	7.434	2.021	0.1643	1.31	5.1
KW-29	0.512777	7	6.104	1.784	0.1767	1.54	4.8
KW-30	0.512698	4	6.248	1.777	0.1720	1.65	3.8
KW-31	0.51277	6	5.280	1.598	0.1830	1.88	4.0
KW-32	0.512763	5	6.252	1.852	0.1790	1.70	4.3
KW-34	0.512777	6	5.473	1.622	0.1791	1.64	4.6
WJS-1	0.512513	5	11.60	2.966	0.1546	1.64	2.0
WJS-1-CPX	0.512668	4	14.84	4.556	0.1856	2.60	1.8
WJS-1-PL	0.512347	6	13.09	2.669	0.1232	1.35	2.0
WJS-2	0.512551	11	6.313	1.695	0.1624	1.77	1.9
WJS-3	0.512556	5	7.576	1.934	0.1543	1.52	2.9
WJS-4	0.512576	5	14.83	3.641	0.1485	1.34	3.9
WJS-6	0.512711	8	7.266	2.096	0.1744	1.70	3.8

CPX: clinopyroxene; PL: plagioclase.

Xixiang and the Tiechuanshan rocks indicates tectonic transition from subduction to intra-continental rift and thus from amalgamation to beak-up of the Rodinia in South China onset at ~820 Ma.

As discussed above, the remarkably higher MgO, Cr and Ni and lower incompatible element concentrations of the Wangjiangshan Gabbros compared to coeval southeastern Australian Gairdner Dyke imply a higher degree of partial melting of the source mantle and accordingly a higher geotherm. If so, the head of the assumed Neoproterozoic plume, which broke the Rodinia, should have centered beneath South China (Li et al., 1999).

The intra-continental rift igneous suites are covered unconformably by the late Sinian tuff, tillite, carbonate, phosphorite and black shale in South China. The tuff was dated at 748 ± 12 Ma by the SHRIMP U–Pb zircon method (Ma et al., 1984). The late Sinian succession may reflect rapid subsidence and formation of passive margins (Gao et al., 1996). The overall Neoproterozoic basin development in South China is analogous to the Adelaide Geosyncline (e.g. Zhao et al., 1994; Barovich and Foden, 2000) (Tables 6 and 7).

8. Conclusions

(1) The lower and upper volcanic units of the Xixiang Group are dated at 950 ± 4 and 897 ± 3 Ma, respectively, whereas the Tiechuanshan bimodal volcanic suite is considerably younger dated at 817 ± 5 Ma.
(2) Boninitic andesites and low-Ti basalts characterize the lower Xixiang unit, indicating a fore-arc setting for their formation. In contrast, basalts and rhyolites from the upper Xixiang unit display similar positive ε_{Nd} (t) and arc-geochemical signatures suggesting a back-arc setting for their genesis.
(3) The Tiechuanshan Formation is a bimodal basalt and dacite–rhyolite suite. This formation may be formed within continental rift caused by plume activity.
(4) The remarkably higher MgO, Cr and Ni and lower incompatible element concentrations of the Wangjiangshan Gabbro compared to coeval southeastern Australian Gairdner Dyke imply a higher degree of partial melting of the source mantle and accordingly a higher geotherm.

(5) The age and geochemical and isotopic contrasts between the Xixiang and the Tiechuanshan volcanic rocks indicate a tectonic transition from subduction at 950–900 Ma (thus the amalgamation of Rodinia) to intra-continental rift (thus the onset of Rodinia break-up) at ca. 820 Ma.

Acknowledgements

We thank X.-H. Li and Z.-X. Li for helpful discussions and S. Jung and M. Sun for constructive reviews. This study was supported by the National Science Foundation of China (Grants 49873010, 49794043, 49573138, 40133020) and a Senior Visitor Fellowship of Chinese Academy of Science to W.L.

References

Albarède, F., 1992. How deep do common basaltic magmas form and differentiate? J. Geophys. Res. 97, 10997–11009.

Allen, C.M., 2000. Evolution of a post-batholith dike swarm in central coastal Queensland, Australia: arc-front to backarc? Lithos 51, 331–349.

Ames, L., Zhou, G., Xiong, B., 1996. Geochronology and geochemistry of ultrahigh-pressure metamorphism with implications for collision of the Sino-Korean and Yangtze cratons, central China. Tectonics 15, 472–489.

Arculus, R.J., Pearce, J.A., Murton, B.J., van der Laan, S.R., 1992. Igneous stratigraphy and major-element geochemistry of Holes 786a and 786b. Proc. Ocean Drill. Prog. Sci. Results 125, 143–169.

Arndt, N.T., Christensen, U., 1992. The role of lithospheric mantle in continental flood volcanism: thermal and geochemical constraints. J. Geophys. Res. 97, 10967–10981.

Arndt, N.T., Chauvel, C., Czamanske, G., Fedorrenko, V., 1998. Two mantle sources, two plumbing systems: tholeiitic and alkaline magmatism of the Maymecha River basin, Siberian flood volcanic province. Contrib. Miner. Petrol. 133, 297–313.

Barovich, K.M., Foden, J., 2000. A Neoproterozoic flood basalt province in southern-central Australia: geochemical and Nd isotope evidence from basin fill. Precambrian Res. 100, 213–234.

Barrat, J.A., Fourcade, S., Jahn, B.M., Cheminée, J.L., Capdevila, R., 1998. Isotope (Sr, Nd, Pb, O) and trace-element geochemistry of volcanism from the Erta'Ale range (Ethiopia). J. Volcanol. Geothermal. Res. 80, 85–100.

Beccaluva, L., Serri, G., 1988. Boninitic and low-Ti subduction-related lavas from intraocanic arc-backarc system and low-Ti ophiolites: a reappraisal of their petrogenesis and original tectonic setting. Tectonophysics 146, 291–315.

Bonin, B., 1996. A-type granite ring complex: mantle origin through crustal filters and the anorthosite-rapakivi magmatism connection. In: Demaiffe, D. (Ed.), Petrology and Geochemistry of Magmatic Suites of Rocks in the Continental and Oceanic Crusts. Université Libre de Bruxelles, Royal Museum for Central Africa (Tervuren), pp. 201–218.

Brown, A.V., Jenner, G.A., 1989. Geological setting, petrology and chemistry of Cambrian boninite and low-Ti tholeiite lavas in western Tasmania. In: Crawford, A.J. (Ed.), Boninites and Related Rocks. Unwin Hyman, London, pp. 232–263.

Cameron, W.E., 1989. Contrasting boninite–tholeiite associations from New Caledonia. In: Crawford, A.J. (Ed.), Boninites and Related Rocks. Unwin Hyman, London, pp. 314–338.

Campbell, I.H., Griffiths, R.W., 1990. Implication of mantle plume structure for the evolution flood basalts. Earth Planet. Sci. Lett. 99, 79–93.

Chen, J.F., Foland, K.A., Xing, F.M., Xu, X., Zhou, T.X., 1991. Magmatism along the southeastern margin of the Yangtze block: Precambrian collision of the Yangtze and Cathaysia blocks of China. Geology 19, 815–818.

Crawford, A. J., Falloon, T. J., Green, D. H., 1989. Classification, petrogenesis and tectonic setting of boninites. In: Crawford, A.J. (Ed.), Boninites and Related Rocks. Unwin Hyman, London, pp. 1–49.

Dalziel, I.W.D., 1991. Pacific margins of Laurentia and East Antarctica–Australia as a conjugate rift pair: evidence and implications for an Eocambrian supercontinent. Geology 19, 598–601.

Davies, G.R., Macdonald, R., 1987. Crustal influences in the petrogenesis of the Naivasha basalt–comendite complex: combined trace element and Sr–Nd–Pb isotope constraints. J. Petrol. 28, 1009–1031.

DePaolo, D.J., Daley, E.E., 2000. Neodymium isotopes in basalts of the southwest basin and range and lithospheric thinning during continental extension. Chem. Geol. 169, 157–185.

DePaolo, D.J., Wasserburg, G.J., 1976. Nd isotopic variations and petrogenetic models. Geophys. Res. Lett. 3, 249–252.

Fan, J., Kerrich, R., 1997. Geochemical characteristics of Al depleted and underpleted komatiites and HREE-enriched tholeiites, western Abitibi greenstone belt: variable HFSE–REE systematics in a heterogeneous mantle plume. Geochim. Cosmochim. Acta 61, 4723–4744.

Foley, S.F., Peccerillo, A., 1992. Potassic and ultrapotassic magmas and their origin. Lithos 28, 181–185.

Frimmel, E., Zartman, R.E., Späth, A., 2001. The Richterveld igneous complex, South Africa: U–Pb zircon and geochemical evidence for the beginning of Neoproterozoic continental break-up. J. Geol. 109, 493–508.

Gallagher, K., Hawkersworth, C.J., 1992. Dehydration melting and the generation of continental flood basalts. Nature 258, 57–59.

Gao, S., Zhang, B.-R., Li, Z.-J., 1990. Geochemical evidence for Proterozoic continental arc and continental margin rift magmatism along the northern margin of the Yangtze Craton, South China. Precambrian Res. 47, 205–221.

Gao, S., Zhang, B.-R., Wang, D.-P., Ouyang, J.-P., Xie, Q.-L., 1996. Geochemical evidence for the Proterozoic tectonic evolution of the Qinling Orogenic Belt and its adjacent margins of the North China and Yangtze cratons. Precambrian Res. 80, 23–48.

Gibson, S.A., Thompson, R.N., Dickin, A.P., 2000. Ferropicrites: geochemical evidence for Fe-rich streaks in upwelling mantle plumes. Earth Planet. Sci. Lett. 174, 355–374.

Goldstein, S.L., O'Nions, R.K., Hamilton, P.J., 1984. A Sm–Nd isotopic study of atmospheric dust and particulates from major river systems. Earth Planet. Sci. Lett. 70, 221–236.

Guan, X.-C., Li, X.-H., Zhao, F.-Q., Wang, Y.-X., 1996. U–Pb and Sm–Nd geochronology of spilites from the Danzhou Group of the Longsheng area, Guangxi Province. Geochimica 25, 270–276 (in Chinese with English abstract).

Hacker, B.R., Ratschbacher, L., Webb, L., Ireland, T., Walker, D., Dong, S., 1998. U/Pb zircon ages constrain the architecture of the ultrahigh-pressure Qinling-Dabie Orogen, China. Earth Planet. Sci. Lett. 161, 215–230.

Hawkesworth, C.J., Lightfood, P.C., Fedorenko, V.A., Blake, S., Naldrett, A.J., Doherty, W., Gorbachev, N.S., 1995. Magma differentiation and mineralisation in the Siberian flood basalts. Lithos 34, 61–88.

Hickey, R.L., Frey, F.A., 1982. Geochemical characteristics of boninite series volcanics: implications for their source. Geochim. Cosmochim. Acta 46, 2099–2116.

Hickey-Vargas, R., 1989. Boninites and tholeiites from the DSDP Site 458, Mariana forearc. In: Crawford, A.J. (Ed.), Boninites and Related Rocks. Unwin Hyman, London, pp. 339–356.

Hickey-Vargas, R., Reagan, M.K., 1987. Temporal variation of isotope and rear earth element abundances in volcanic rocks from Guam: implications for the evolution of the Mariana Arc. Contrib. Miner.. Petrol. 97, 497–508.

Hoffman, P.F., 1991. Did the breakout of Laurentia turn Gondwanaland inside-out? Science 252, 1409–1412.

Hu, S.-H., Chen, A.-F., Lin, S.-L., Yu, H.-L., Gao, S., 2000. ICP-MS analysis of 40 trace and ultra-trace elements in geological samples. J. China Univ. Geosci. 25, 186–190 (in Chinese with English abstract).

Keppie, J.D., Dostal, J., Ortega-Gutiérrez, F., Lopez, R., 2001. A Grenvillian arc on the margin of Amazonia: evidence from the southern Oaxacan Complex, southern Mexico. Precambrian Res. 112, 165–181.

Kerrich, R., Wyman, D., Fan, J., Bleeker, W., 1998. Boninite series: low Ti-tholeiite associations from the 2.7 Ga Abitibi greenstone belt. Earth Planet. Sci. Lett. 164, 303–316.

Krogh, T.E., 1973. A low contamination method for hydrothermal decomposition of zircon and extractions of U and Pb for isotopic age determinations. Precambrian Res. 37, 485–494.

Li, H.-M., Dong, C.-W., Xu, D.-S., Zhou, X.-M., 1995. Petrogenesis of southeastern Fujian mafic intrusions: constraint from the single-grain zircon U–Pb geochronology of Quanzhou Gabbro. Chin. Sci. Bull. 40, 158–160.

Li, X.-H., 1997. Geochemical and Sm–Nd isotopic study of the Longsheng Ophiolite from the southern margin of Yangtze Craton: implications for Proterozoic tectonic evolution in SE China. Geochem. J. 31, 323–337.

Li, X.-H., 1999. U–Pb zircon ages of granites from the southern margin of the Yangtze block: timing of the Neoproterozoic Jinning Orogeny in SE China and implications for Rodinia assembly. Precambrian Res. 97, 43–57.

Li, X.-H., McCulloch, M.T., 1996. Secular variation in the Nd isotopic composition of Neoproterozoic sediments from the southern margin of the Yangtze Block: evidence for a Proterozoic continental collision in south China. Precambrian Res. 76, 67–76.

Li, X.-H., Zhou, G.Q., Zhao, J.X., Fanning, C.M., Compston, W., 1994. SHRIMP ion microprobe zircon age and Sm–Nd isotopic characteristics of the NE Jiangxi ophiolite and its tectonic implications. Chin. J. Geochem. 13, 317–325.

Li, X.-H., Zhao, J.X., McCulloch, M.T., Zhou, G.Q., Xing, F.M., 1997. Geochemical and Sm–Nd isotopic study of Late Proterozoic ophiolites from southeastern China: petrogenesis and tectonic implications. Precambrian Res. 81, 129–144.

Li, X.-H., Li, Z.X., Zhou, H.-W., Liu, Y., Kinny, P., 2002. U–Pb zircon geochronologic, geochemical and Nd isotopic studies of Neoproterozoic bimodal volcanism in the Kangdian Rift of South China: implications for the initial rifting of Rodinia. Precambrian Res. 113, 135–155.

Li, Z.X., Zhang, L., Powell, C.McA., 1995. South China in Rodinia: part of the missing link between Australia–East Antarctica and Laurentia? Geology 23, 407–410.

Li, Z.X., Zhang, L., Powell, C.McA., 1996. Positions of the East Asian cratons in the Neoproterozoic supercontinent Rodinia. Aust. J. Earth Sci. 43, 593–604.

Li, Z.X., Li, X.-H., Kinny, P.D., Wang, J., 1999. The break-up of Rodinia: did it start with a mantle plume beneath South China? Earth Planet. Sci. Lett. 173, 171–181.

Ling, W.-L., 1996. Geochronology and crustal accretion of the Proterozoic basements in the northern margin of Yangtze craton: I. Houhe and Xixiang Groups. Earth Sci. 21, 491–494 (in Chinese with English abstract).

Ling, W.-L., Gao, S., Zhang, B.-R., Zhou, L., Zhang, H.-F., 1997. Early Precambrian evolution of the crust in the northern margin of Yangtze craton, constrained by the case study of Houhe Complex. J. Miner. Rocks 17, 26–32 (in Chinese with English abstract).

Liu, D.-Z., Wei, X.-G., Du, S.-C., Xu, X.-H., 1997. Advance of geologic survey in western Micangshan region. J. Miner. Rock. 17(Suppl.), 1–8 (in Chinese with English abstract).

Ludwig, R.K., 1998. ISOPLOT: A Plotting and Regression Program for Radiogenic-Isotope Data, Version 2.96. US Geological Survey Open File Report (91-445), 46 pp.

Ma, G., Lee, H., Zhang, Z., 1984. An investigation of the age limits of the Sinian System in South China. Bull. Yichang Inst. Geol. Miner. Resour. 8, 1–29 (in Chinese with English abstract).

McKenzie, D., Bickle, M.J., 1988. The volume and composition of melt generated by extension of the lithosphere. J. Petrol. 29, 625–679.

Meffre, S., Aitchison, J.C., Crawford, A.J., 1996. Geochemical evolution and tectonic significance of boninites and tholeiites from the Koh ophiolite. New Caledonia. Tectonics 15, 67–83.

Middlemost, E.A.K., 1994. Naming materials in the magma/igneous rock system. Earth-Sci. Rev. 37, 215–224.

Mingram, B., Trumbull, R.B., Littman, S., Gerstenberger, H., 2000. A petrogenetic study of anorogenic felsic magmatism in the Cretaceous Paresis ring complex, Namibia: evidence for mixing of crust and mantle-derived components. Lithos 54, 1–22.

Montel, J.M., Vielzeuf, D., 1997. Partial melting of greywackes: Part II. Composition of minerals and melts. Contrib. Miner.. Petrol. 128, 176–196.

Moores, E.M., 1991. Southwest U.S.–East Antarctic (SWEAT) connection: a hypothesis. Geology 19, 425–428.

Pearce, J.A., Harris, N.B.W., Tindle, A.G., 1984. Trace element discrimination diagrams for the tectonic interpretation of granitic rocks. J. Petrol. 25, 956–983.

Pearce, J.A., Thirlwall, M.F., Imgram, G., Murton, B.J., Arculus, R.J., van der Laan, S.R., 1992. Isotopic evidence for the origin of boninites and related rocks drilled in the Izu-Bonin (Ogasawara) forearc, Leg 125. Proc. Ocean Drill. Prog. Sci. Results 125, 237–261.

Piercey, S.J., Murphy, D.C., Mortensen, J.K., Paradis, S., 2001. Boninitic magmatism in a continental margin setting, Yukon-Tanana terrane, southeastern Yukon, Canada. Geology 29, 731–734.

Rickers, K., Mezger, K., Raith, M.M., 2001. Evolution of the continental crust in the Proterozoic Eastern Ghats Belt, India and new constraints for Rodinia reconstruction: implications from Sm–Nd, Rb–Sr and Pb–Pb isotopes. Precambrian Res. 112, 183–210.

Rudnick, R.L., Fountain, D.M., 1995. Nature and composition of the continental crust: a lower crust perspective. Rev. Geophys. 33, 267–309.

Shinjo, R., 1999. Geochemistry of high Mg andesites and the tectonic evolution of the Okinawa Trough–Ryukyu arc system. Chem. Geol. 157, 69–88.

Stern, C.R., Kilian, R., 1996. Role of the subducted slab, mantle wedge and continental crust in the generation of adakites from the Andean Austral Volcanic Zone. Contrib. Miner. Petrol. 123, 263–281.

Sun, S.-S., McDonough, W.F., 1989. Chemical and isotopic systematics of oceanic basalts: implications for mantle composition and processes. In: Saunders, A.D., Norryt, M.J. (Eds.), Magmatism in the Ocean Basins. Geol. Soc. Spec. Publ. 42, 313–345.

Togashi, S., Imai, N., Okuyama-Kusunose, Y., Tanaka, T., Okai, T., Koma, T., Murata, Y., 2000. Young upper crust chemical composition of the orogenic Japan Arc. Geochem. Geophys. Geosyst. 1, 2000GC00083.

Turner, S., Arnaus, N., Liu, J., Rogers, N., Hawkesworth, C., Harris, N., Kelley, S., Van Calsteren, P., Deng, W., 1996. Post-collision, shoshonitic volcanism on the Tibetan Plateau: implications for convective thinning of the lithosphere and source of ocean island basalts. J. Petrol. 37, 45–71.

Vance, D., Strachan, R.A., Jones, K.A., 1998. Extensional versus compressional settings for metamorphism: garnet chronometry and pressure–temperature–time histories in the Moine Supergroup, northwest Scotland. Geology 26, 927–930.

Whalen, J.B., Currie, K.L., Chappell, B.W., 1987. A-type granites: geochemical characteristics, discrimination and petrogenesis. Contrib. Miner.. Petrol. 95, 407–419.

Wilson, W., 1989. Igneous Petrogenesis. Unwin Hyman, London, pp. 327–373.

Winchester, J.A., Floyd, P.A., 1976. Geochemical magma type discrimination: application to altered and metamorphosed igneous rocks. Earth Planet. Sci. Lett. 28, 459–469.

Wingate, M.T.D., Campell, I.H., Compston, W., Gibson, G.M., 1998. Ion microprobe U–Pb ages for Neoproterozoic basaltic magmatism in south-central Australia and implications for the break-up of Rodinia. Precambrian Res. 87, 135–159.

Wyman, D., 1999. A 2.7 Ga depleted tholeiite suite: evidence of plume–arc interaction in the Abitibi Greenstone belt. Canada. Precambrian Res. 97, 27–42.

Xia, Z.-C., Luo, C.-Y., Wang, J.-L., Liu, W.-F., Zhang, G.-F., Li, Z.-P., 1988. Wangjiangshan mafic intrusion: an example of multi-stage magma streaming and mixing. Bull. Xi'an Inst. Geol. Miner. Resour. 22, 1–20 (in Chinese with English abstract).

Xie, Z., Chen, J.-F., Zheng, Y.-F., Zhang, X., Li, H.-M., Zhou, T.-X., 2001. Zircon U–Pb dating of the metamorphic rocks of different grades from the southern part of the Dabie terrain in China. Phys. Chem. Earth (A) 26, 685–693.

Yogodzinski, G.M., Kay, R.W., Volynets, O.N., Koloskov, A.V., Kay, S.M., 1995. Magnesian andesite in the western Aleutian Komandorsky region: implications for slab melting and processes in the mantle wedge. Geol. Soc. Am. Bull. 107, 505–519.

Zhang, R.-P., 1991. Geological Map of Qingling-Dabie Mountains and Adjacent Region of the People's Republic of China (1:1000000). Geological Publishing House, Beijing.

Zhang, Z.-Q., Zhang, G.-W., Fu, G.-M., Tong, S.-H., Song, B., 1997. A geochronological study of metamorphosed sedimentary and volcanic rocks from Qinling orogenic belt and their tectonic significances. Sci. China, Ser. D 26, 216–222.

Zhang, Z.-Q., Zhang, G.-W., Tang, S.-H., Zhang, Q.-D., Wang, J.-H., 2000. Geochronology of the Hannan intrusive complex adjacent to the Qinling orogen and its rapid cooling history. Chin. Sci. Bull. 46, 685–689.

Zhou, X.-M., Zou, H.-B., Yang, J.-D., Wang, Y.-X., 1990. Sm–Nd isochronous age of Fuchuan Ophiolite suite in Shexian county, Anhui Province, and its geological significance. Chin. Sci. Bull. 35, 208–212.

Zhao, J.X., McCulloch, M.T., Korsch, R.J., 1994. Characterisation of a plume-related ~800 Ma magmatic event and its implications for basin formation in central-southern Australia. Earth Planet. Sci. Lett. 121, 349–367.